

IMPERIAL

Spirals, defects, rolls and bands;
**Transitional Rayleigh-Bénard Poiseuille flows
using spectral/*hp* element methods**

BY

Chi Hin Chan

SUPERVISED BY

Professor Spencer J. Sherwin
&
Professor Yongyun Hwang

at the

DEPARTMENT OF AERONAUTICS
FACULTY OF ENGINEERING
IMPERIAL COLLEGE LONDON

THIS THESIS IS SUBMITTED FOR THE DEGREE OF DOCTOR OF PHILOSOPHY

Declarations

Statement Of Originality

I certify that the content of this thesis is a product of my own work. I have appropriately acknowledged any other material that may have been used through standard referencing practices.

Copyright Declaration

The copyright of this thesis rests with the author. Unless otherwise indicated, its contents are licensed under a Creative Commons Attribution-Non Commercial 4.0 International Licence (CC BY-NC). Under this licence, you may copy and redistribute the material in any medium or format. You may also create and distribute modified versions of the work. This is on the condition that: you credit the author and do not use it, or any derivative works, for a commercial purpose. When reusing or sharing this work, ensure you make the licence terms clear to others by naming the licence and linking to the licence text. Where a work has been adapted, you should indicate that the work has been changed and describe those changes. Please seek permission from the copyright holder for uses of this work that are not included in this licence or permitted under UK Copyright Law.

Abstract

The transitional regimes of Rayleigh-Bénard Poiseuille (RBP) flows and Rayleigh-Bénard convection (RBC) are investigated using direct numerical simulations and linear stability analysis. RBP flows serve as a paradigmatic configuration that describes fluid motion driven by shear and buoyancy forces, a combination of the classical buoyancy-driven RBC and shear-driven plane Poiseuille flow (PPF). While the transitional regime of RBC and PPF have been well studied over the past century, the transitional regime where both forces interact remains largely unexplored beyond linear instability.

Following a review of the relevant literature and numerical methods, we conduct direct numerical simulations of transitional RBP flows using Nektar++, a spectral/ hp element package. The simulations span over a range of Rayleigh numbers, $Ra \in [0, 10000]$ and Reynolds number $Re \in [0, 2000]$, with unit Prandtl number in a large computational domain. Within this parametric space, we identify five distinct regimes: (1) bistable SDC & ISRs, (2) ISRs, (3) wavy rolls, (4) intermittent rolls, and (5) shear-driven turbulence. The (4) intermittent rolls regime represent a newly identified state characterised by the spatio-temporal intermittent breakdown and regeneration of longitudinal rolls. In the (5) shear-driven turbulent regime, we also observe that intermittent rolls may coexist with turbulent-laminar bands. The spatio-temporal intermittent dynamics of longitudinal rolls highlight its dominant role in transitional RBP flows. To suppress spatial intermittency, we examine the unstable manifolds of the longitudinal rolls in a confined domain, integrating along which leads to turbulence. Depending on Re , this turbulence may occur transiently, decaying towards the unstable laminar base state where the longitudinal rolls can be excited again, forming a quasi-cyclic process referred to as the *thermally-assisted sustaining process (TASP)*. We furnish a state space sketch of the dynamical process, and discuss the relevance of the *TASP* to larger domains, concluding the first part of the thesis.

In the second part, we explore the state space structure of the bistable system between spiral defect chaos (SDC) and ideal straight rolls (ISRs) of Rayleigh-Bénard convection within large domains. By systematically reducing the domain size, we observe that SDC occurs transiently, eventually stabilising into multiple stable invariant solutions, referred to as *elementary states*. These *elementary states* are visually and statistically similar to the localised features of SDC, underpinning the pattern formation of SDC. We also examined the edge between the basin of attractions of ISRs and the elementary states, revealing multiple edge states. Investigating the unstable manifolds of ISRs exhibit two distinct behaviours: (1) unstable ISRs near the Busse balloon connect to stable ISRs and base state via heteroclinic connections, and (2) unstable ISRs further from the Busse balloon lead to SDC, indicating such ISRs lie on boundary between ISRs and SDC. Finally, we present a state space sketch of the *elementary states* organised around SDC, highlighting its ‘building-block’ description of SDC.

Acknowledgements

There are many people who have shaped my experience as a PhD student whom I would like to express my gratitude for. First and foremost, I want to express my deepest gratitude to my supervisors, Spencer and Yongyun. I have learned and grown a lot under their tremendously kind and patient supervision. It is a truly a pleasure to learn from world leading experts in fluid mechanics and computational fluid dynamics, and I will miss the knowledge osmosis process during our weekly catch-ups. Apart from the PhD, they also openly supported personal development opportunities, allowing me to pursue interests such as the Nektar++ redesign project, engaging in graduate teaching assistant roles, pursuing a summer research exchange at LadHyX and an internship at IBM Research, which I am grateful for.

I would like to specially thank Yongyun, who also happens to be my MSc thesis supervisor. Together, we worked the topic of reduced-order modelling of turbulent Couette flows as part of my MSc thesis. Perhaps more importantly, for giving me the confidence I needed to pursue a PhD program at Imperial.

I would also like to thank Lutz, for his kind hospitality, ensuring that I was comfortable at LadHyX in the summer of 2024. Despite being a short three months stint, I learned about advanced modal decomposition techniques and was exposed to the broad fluid mechanics research activities at LadHyX.

I would also like to thank Basman, my Bachelor's thesis supervisor at Nanyang Technological University (NTU), during which we worked on humpback whale leading-edge tubercles for my FYP. I believe it is fair to say that he was primarily responsible for planting the "seed" for my fascination for computational fluid dynamics.

I would also like to thank the Nektar++ community, particularly Henrik, Alex, Chris, Jacques and Dave for their timely responses on compilation errors, segmentation faults and guidance on software principles for contributing to Nektar++.

I would also like to thank my collaborators, Mohammad and Raj, for providing invaluable guidance and advice during the PhD, and also the opportunity to collaborate on physics-informed neural networks.

I would like to also thank Eloisa and Geeth, my project supervisor and manager at IBM Research, for giving an eye-opening opportunity to learn and contribute to AI research activities in a corporate company.

I would thank my fellow PhD students and postdocs from the office, for their endearing support over the 'instabilities' of PhD and London life. I will fondly remember our shared experiences such as unwinding over a cheeky pint on Friday evenings, mario karting in the common room, going to Sagar and exploiting its 50% discount, honest burgers student discounts, going to Wasabi at South

Kensington at closing to get half-priced bentos, countless muffin (Toffee banana is the best) and coffee breaks, peaceful walks around campus, Hyde park runs, booking the swimming pool sessions just to use the sauna, many gym/swim/badminton/climbing sessions, appearing decently surprise to bump into each other in the office on the weekends, and bantering over the weather, reviewers and PhD life. Special thanks to Henrik, Parv, Alex, Kaloyan, Ganlin, Steffi, Lidia, Christian, Kazuki, Priyam, Sid, Elise, Yu Hang, Cheng Wei, Zhao, Zilin, Victor, Mohsen, Guglielmo, João, Yacine and many others, all of whom made London feel like home.

The person who probably deserves the most credit would be my fiancée, Angelica, who have been there at the beginning, ready to lend a listening ear to my monologue on how cool CFD is. The distance between Singapore and London has been tough over the years, and I look forward to building our shared future after the PhD. Last but not least, I am grateful to my loving parents and family, for supporting my academic interests and developments aboard despite the distance.

I would like to acknowledge the generous financial support from the Imperial College President's PhD scholarships, Global Fellows Fund and computing resources from ARCHER2, without which this PhD would not have been possible.

Chi Hin Chan
London
November 2025

Contents

1	The state space structure of SDC	1
1.1	Objectives	1
1.2	Problem formulation	2
1.2.1	Rayleigh-Benard convection (RBC)	2
1.2.2	Numerical method	3
1.2.3	Linear stability analysis of ISRs	3
1.3	Transient SDC & elementary states	5
1.4	Multiplicity of edge states	11
1.5	Unstable ideal straight rolls	18
1.5.1	Pathways leading to ISRs - heteroclinic orbits	20
1.5.2	Pathways leading to elementary states	22
1.5.3	A pathway to SDC in an extended domain $\Gamma = 4\pi$	24
1.6	Summary	26
A	Appendices	29
A.1	Simulation parameters for <i>Ra-Re</i> sweep	29
A.2	1st and 2nd order statistics	29
A.2.1	Buoyancy-driven regime	29
A.2.2	Shear-driven regime	32
A.3	Growth rates of primary instabilities	32
A.4	Verification of linear stability analysis	35
A.5	Other elementary states and ISRs	35

Chapter 1

The state space structure of Spiral Defect Chaos

The co-existence of ideal straight rolls (ISRs) and spiral-defect chaos (SDC) as bistable states in Rayleigh-Bénard convection above the onset of the linear instability is well established in extended spatial domains ($\Gamma \geq 40$ where Γ is the aspect ratio of the domain). However, multiple stable states have also been found independently, raising questions about the precise understanding of this observed bistability in extended domains. In this study, we isolate the localised structures of SDC by gradually reducing the spatial domain. By minimising the domain systematically to $\Gamma = 2\pi$, SDC appears transiently and eventually stabilises into new stable states referred to as elementary states. These elementary states are visibly and statistically similar to the spatially local patterns of SDC, indicative of invariant solutions underpinning the pattern formation in SDC.

To understand the state space structure further, we have examined the edge between ISRs and the elementary states, revealing multiple edge states, and conducted a series of numerical simulations along the unstable manifolds of unstable ISRs. The unstable ISRs near the Busse balloon are connected to stable ISRs and the base state through networks of heteroclinic orbits, forming a basin of attraction for each stable ISR. In contrast, the unstable ISRs further from the Busse balloon contain some unstable manifolds, along which the solution trajectory leads to SDC, suggesting that these unstable ISRs sit on the boundary between stable ISRs and SDC. Finally, we propose a state-space structure around the basic heat conduction state, stable/unstable ISRs, elementary states and transient SDC.

1.1 Objectives

The bistability between SDC and ISR is well established, but this also opens a question of how it is connected with the previous findings of multiple stable states (see §??). It is worth noting that a possible parameter in exploring this connection appears to be the domain size. Bistability has been reported in domains much larger ($\Gamma = 50$) than the multiple states found in small-to-moderate domains ($\Gamma \leq 10$) ([Cakmur, Egolf, Plapp, & Bodenschatz, 1997](#)). Furthermore, giant rotating spirals have been found in domains comparable to the horizontal length scale of SDC ([Plapp & Bodenschatz, 1996](#); [Plapp, Egolf, Bodenschatz, & Pesch, 1998](#)). Under this premise, the scope of this study is to explore

how SDC, ISRs and multiple states are organised within a state space, where stable/unstable equilibria and their manifolds (or linear stability) could provide useful physical insights into the state transition dynamics.

Motivated by the observation that SDC consists of several localised structures that resemble multiple states (i.e. travelling waves, spirals, asymmetric states), we first seek to isolate these states by minimising the domain systematically. Confined within the minimal domain, SDC is found to appear only transiently and does not sustain for a long time. The transient SDC state eventually stabilises into a large number of stable multiple states, which will be referred to as the ‘elementary’ states of SDC, and they are subsequently found within the minimal domain. As we shall see later, these elementary states remarkably resemble local structures of SDC observed in wide computational domains, indicating that they possibly underpin the formation of SDC. Next, the state-space boundaries between SDC and ISRs are explored by employing the edge-tracking technique ([Schneider, Eckhardt, & Yorke, 2007](#); [Skufca, Yorke, & Eckhardt, 2006](#)), unveiling the existence of multiple edge states sitting on the boundaries. Finally, to understand the role of the unstable ISRs outside the Busse balloon, we perform a series of numerical experiments, in which a small perturbation is added along the unstable manifolds of several (unstable) ISRs outside of the Busse balloon. We shall see that some of their unstable manifolds are connected to stable ISRs within the Busse balloon, while the others are linked to transient SDC, which is subsequently stabilised into an elementary state. This suggests that some of the unstable ISRs act as signposts for the state-space boundary between stable ISRs and SDC (and/or elementary states).

The main contributions of the present chapter can be briefly summarised as follows,

1. Discovery of a number of stable invariant solutions which underpin the localised structures of SDC by minimising the computational domain for SDC (section [1.3](#));
2. Computation of some of multiple ‘edge states’ sitting on the separatrix between SDC and ISRs (section [1.4](#));
3. Several heteroclinic orbits connecting unstable ISRs and stable ISRs near the boundaries of the Busse balloon (section [1.5.1](#));
4. The role of unstable ISRs far from the Busse balloon acting as a signpost between ISRs and SDC (section [1.5.2](#)).

1.2 Problem formulation

1.2.1 Rayleigh-Benard convection (RBC)

The motion of fluid flow in an RBC system (see [§??](#)), is governed by the non-dimensionalised Navier-Stokes equations with Boussinesq approximation,

$$\frac{\partial \mathbf{u}}{\partial t} + (\mathbf{u} \cdot \nabla) \mathbf{u} = -\nabla p + Pr \nabla^2 \mathbf{u} + Ra Pr \theta \mathbf{j}, \quad (1.1a)$$

$$\frac{\partial \theta}{\partial t} + (\mathbf{u} \cdot \nabla) \theta = \nabla^2 \theta, \quad (1.1b)$$

$$\nabla \cdot \mathbf{u} = 0, \quad (1.1c)$$

with the following boundary conditions at the wall,

$$\mathbf{u}|_{y=0,1} = 0, \quad \theta|_{y=0} = 1, \quad \theta|_{y=1} = 0, \quad (1.2a)$$

and the periodic boundary condition in the horizontal direction. Here, t denotes the time scaled by the vertical thermal diffusion time, d^2/κ , and $\mathbf{x} (= (x, y, z))$ is the spatial coordinates non-dimensionalised by d , where x and z are two orthogonal horizontal directions and y is the vertical direction. $\mathbf{u} (= (u, v, w))$ is the velocity vector scaled with κ/d , p the pressure scaled with $\rho\kappa^2/d^2$, $\theta (\equiv (T - T_U)/\Delta T)$ the non-dimensional temperature with T being the absolute temperature, and \mathbf{j} denotes the unit vector in y -direction. The Rayleigh number and the Prandtl numbers are defined as in §???: $Ra = \alpha gd^3\Delta T/\nu\kappa$, Prandtl number $Pr = \nu/\kappa$. $Pr = 1$ is set. We note that the aspect ratio is redefined as $\Gamma = L/d$ in this section.

1.2.2 Numerical method

The governing equations are solved numerically using Nektar++, an open-source spectral/ hp -element method framework (Cantwell et al., 2015; Moxey et al., 2020). An initial computational mesh, composed of quadrilateral elements, in the x - y plane is generated using Gmsh (Geuzaine & Remacle, 2009) and then refined by Nekmesh, the mesh generator available in Nektar++. Several computational domains of different sizes are prepared: $(L_x, L_y, L_z) = (16\pi, 1, 16\pi), (8\pi, 1, 8\pi), (4\pi, 1, 4\pi), (2\pi, 1, 2\pi)$. The spatial domain is discretised using a quasi-3D approach with spectral/ hp elements in x - y domain and Fourier expansions in z -direction. The discretised equations are subsequently solved using a velocity-correction method based on a second-order implicit-explicit temporal scheme (see §??). Since different computational domain sizes were considered, the spatial distribution of spectral/ hp elements in the x - y plane and Fourier expansions along z was kept constant. A spatial resolution of $(\Delta x, \Delta y|_{y=0,d}, \Delta y|_{y=d/2}, \Delta z) = (0.1\pi, 0.0549, 0.367, 0.25\pi)$ with polynomial order $P = 4$, and temporal resolution of $\Delta t = 0.0125$ was sufficient to establish numerical independence – for example, the Nusselt number, $Nu (= - \int_{x,z} \frac{\partial \theta}{\partial y}|_{y=0} dx dz)$, varies less than 10^{-5} when P was increased to $P = 5$.

1.2.3 Linear stability analysis of ISRs

As discussed in §1.1, we will perform a set of numerical experiments, in which a small perturbation about several unstable ISRs is added along their unstable manifolds. To obtain the direction of the unstable manifolds (i.e. linear instability eigenfunctions), we consider a small perturbation about the ISR (base) state:

$$\mathbf{u}(\mathbf{x}, t) = \mathbf{u}_{ISR,q}(\mathbf{x}) + \mathbf{u}'(\mathbf{x}, t), \quad (1.3a)$$

$$\theta(\mathbf{x}, t) = \theta_{ISR,q}(\mathbf{x}) + \theta'(\mathbf{x}, t), \quad (1.3b)$$

$$p(\mathbf{x}, t) = p_{ISR,q}(\mathbf{x}) + p'(\mathbf{x}, t), \quad (1.3c)$$

where $\mathbf{s} = [\mathbf{u}, \theta, p]^T$, $\mathbf{s}_{ISR,q} = [\mathbf{u}_{ISR,q}, \theta_{ISR,q}, p_{ISR,q}]^T$ and $\mathbf{s}' = [\mathbf{u}', \theta', p']^T$ refers to solution vector, the ISR (base) state of a given wavenumber, q , and the perturbation respectively. The theoretical background of this section is discussed earlier in §??, and its numerical technique is presented in §??. Substitution of (1.3) into (1.1) leads to the following linearised equations:

$$\frac{\partial \mathbf{s}'}{\partial t} = \mathcal{A}(\mathbf{s}_{ISR,q}; Ra, Pr)\mathbf{s}', \quad (1.4a)$$

where

$$\mathcal{A}(\mathbf{s}_{ISR,q}; Ra, Pr) = \begin{pmatrix} -(\mathbf{U} \cdot \nabla) - (\nabla \mathbf{U} \cdot) + Pr\nabla^2 & RaPr\hat{\mathbf{j}} & -\nabla \\ -(\nabla \Theta \cdot) & -(\mathbf{U} \cdot \nabla) + \nabla^2 & 0 \\ \nabla \cdot & 0 & 0 \end{pmatrix}. \quad (1.4b)$$

For the sake of simplicity here, we will only consider the ISRs invariant along z -direction. Since the ISRs are also assumed periodic in x -direction, the following form of normal-mode solution can be considered:

$$\mathbf{s}'(\mathbf{x}, t) = \check{\mathbf{s}}(x, y)e^{i(\alpha x + \beta z) + \lambda t} + \text{c.c}, \quad (1.5)$$

where λ, α and β are the complex frequency, the streamwise wavenumber (or the Floquet exponent), and the spanwise wavenumber, respectively. Using the periodic nature of $\check{\mathbf{s}}(x, y)$ in x -direction, (1.5) can also be written as

$$\mathbf{s}'(\mathbf{x}, t) = \left[\sum_{n=-\infty}^{\infty} \check{\mathbf{s}}_n(y) e^{i \frac{2\pi}{L_x} (n+\epsilon)x} \right] e^{i\beta z + \lambda t} + \text{c.c}, \quad (1.6)$$

where $\epsilon (= \alpha L_x / (2\pi))$ is the Floquet detuning parameter with $0 \leq \epsilon \leq 1/2$. Since the stability analysis here will be limited to the identification of unstable manifolds of ISRs in a fixed computational domain, $\epsilon = 0$ (fundamental mode) is considered only - note that the modes associated with $\epsilon \neq 0$ are only observed in the x domains greater than L_x .

Substituting (1.6) into (1.4) leads to a discretised eigenvalue problem in terms of the eigenvalue λ , where the wavenumber in the z -direction must be restricted to be $\beta = 2\pi m / L_z$, and m is a positive integer, for the given computational domain. The resulting eigenvalue problems are solved using a time-stepper-based iterative Arnoldi algorithm (see ??). The eigenvalues of primary instabilities of RBC computed in Nektar++ are also verified against those obtained with a Chebyshev-collocation method in Appendix A.4.

1.3 Transient SDC and elementary states in minimal domain

In this section, we seek to capture localised structures of SDC using a minimal domain by systematically reducing the domain by half in the homogeneous (x - z) directions. A random noise, characterised by Gaussian white noise (0 mean and 1 variance), generated with a total energy of

$$\delta = \frac{1}{\bar{V}} \int_{\Omega} \tilde{\mathbf{u}}(\mathbf{x})^T \tilde{\mathbf{u}}(\mathbf{x}) + RaPr\tilde{\theta}(\mathbf{x})^2 d\Omega \approx O(10^{-3}), \quad (1.7)$$

where $\tilde{\mathbf{u}}(\mathbf{x})$ and $\tilde{\theta}(\mathbf{x})$ refer to the perturbation velocity and temperature about the base state $\mathbf{U}(\mathbf{x}) = \mathbf{0}$ and $\Theta(y) = 1 - y$, is introduced as an initial condition to the system. Here, we note that the first term of the integrand in (1.7) is the kinetic energy of the perturbation velocity and the second one measures the potential energy from the perturbation temperature.

The system is time integrated for 300 units of vertical thermal diffusion time t ($= d^2/\kappa$). The resulting mid-plane temperature snapshots $\theta(x, z)|_{y=d/2}$ at $t = 300$ exhibit features of spiral defect chaos, as shown in figure 1.1. When the domain size is large, for instance, $\Gamma = 16\pi$ shown in figure 1.1(a), features of SDC consist of many repeating localised spirals, defects and dislocations. Reducing the domain in half to $\Gamma = 8\pi$, shown in figure 1.1(b), led to a spatially less extensive chaotic state, revealing a single spiral, with some defects and dislocations. Surprisingly, a further reduction of the domain in half, $\Gamma = 4\pi$, does not lead to sustained SDC, but rather, a transient SDC state before settling into stable ‘elementary’ states. These elementary states are identified as *pacman* (PM), *spiral-defect* (SD), *hooked* (HK), and *peanut* (PN) states in figure 1.1 (c-f), which resemble the localised features of SDC (see the coloured bounding boxes in figures 1.1(a,b)). These states represent stable invariant solutions of (1.1). Specifically, PM state represents a steady equilibrium, SD and HK states are characterised by relative periodic orbits ¹, and the PN state is a periodic orbit (Gibson, Halcrow, & Cvitanović, 2008).

An example of a transient SDC state is shown in figure 1.2(a), where spirals, a typical feature of SDC (Morris, Bodenschatz, Cannell, & Ahlers, 1993), form spontaneously with a chaotic transient (figures 1.2(c-e)), before stabilising into an SD state with a period of $T \approx 75$ (figures 1.2(f,g)). In addition to the elementary states presented in figures 1.1(c-f), we have identified ten additional elementary states, each independently preceded by a transient SDC state, and fourteen stable ISRs of varying wavenumbers (see Appendix A.5). We intentionally restrict the spatial domain to identify nontrivial invariant solutions apart from ISRs. This method follows the well-established approach of the minimal flow unit of plane Couette flow (Jiménez & Moin, 1991), where nontrivial solutions within small domains exhibit coherent ‘streak-roll’ structures that reproduce the statistics of turbulent (Kawahara & Kida, 2001). In total, we have identified 28 states with $\Gamma = 4\pi$. Minimising the domain further to $\Gamma = 2\pi$ only led to stable ISRs at least for the random initial conditions we have examined in this study. We therefore consider $\Gamma = 4\pi$ as the minimal domain, in which both transient SDC and elementary states exist. It is worth mentioning that solutions to multiple states were obtained in smaller domains with $\Gamma = 4$, but in a cylindrical domain (Borońska & Tuckerman, 2010a; Ma, Sun,

¹Relative periodic orbit is a type of periodic orbit whereby the solution trajectory after a period T returns to its initial state that is continuously translated in the horizontal directions.

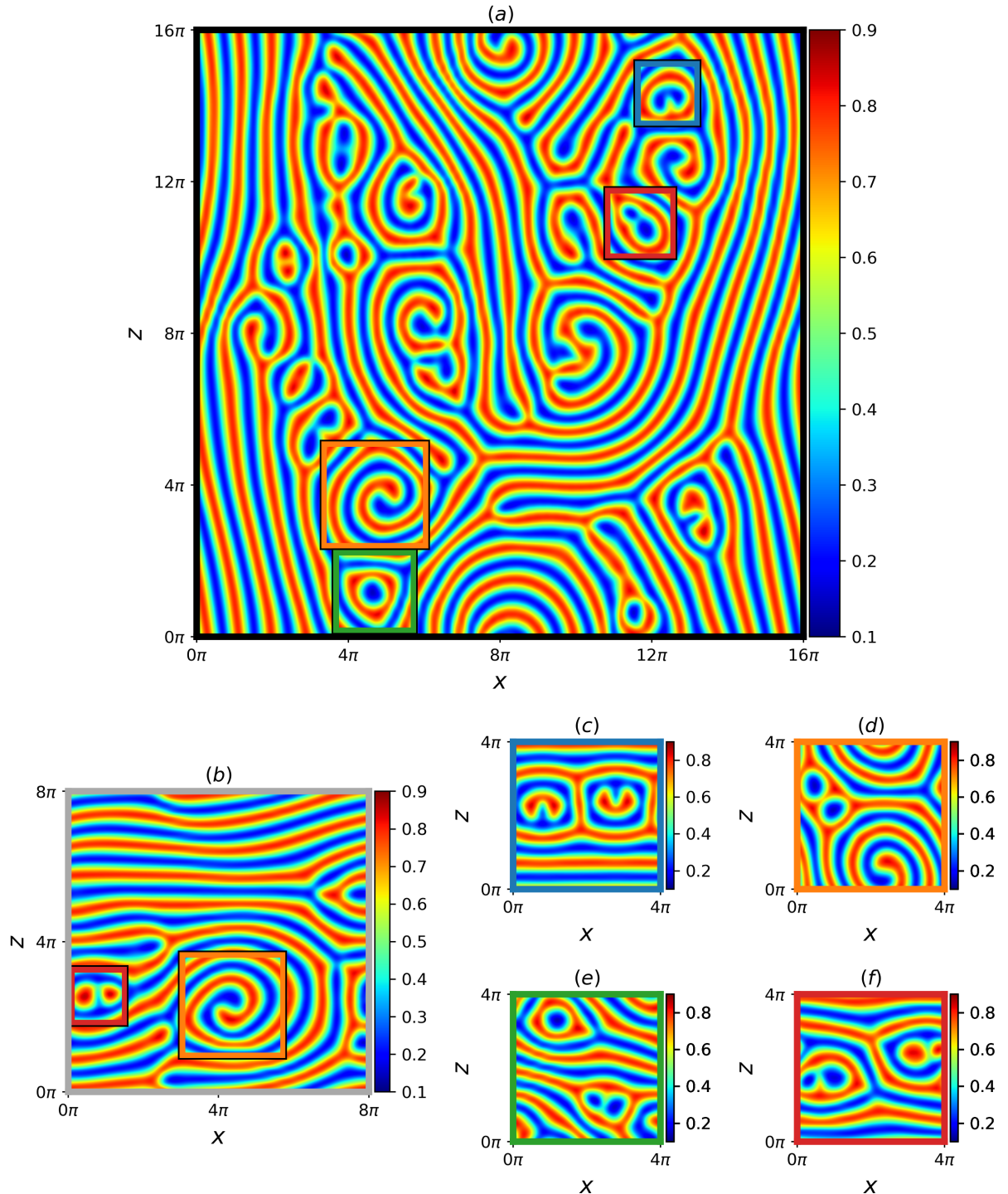


Figure 1.1: Midplane temperature snapshots, $\theta(x, z)|_{y=d/2}$, of spiral defect chaos (SDC) for a domain aspect ratio of (a) $\Gamma = 16\pi$ and (b) 8π . Elementary states of SDC captured when $\Gamma = 4\pi$: (c) steady *pacman* (PM), (d) relative periodic orbit *spiral-defect* (SD), (e) relative periodic orbit *hooked* (HK), and (f) periodic *peanut* (PN) elementary state. Note that the localised structures indicated by bounding boxes in (a,b) resemble structures in (c-f). Snapshots are captured at 300 diffusive time units, t .

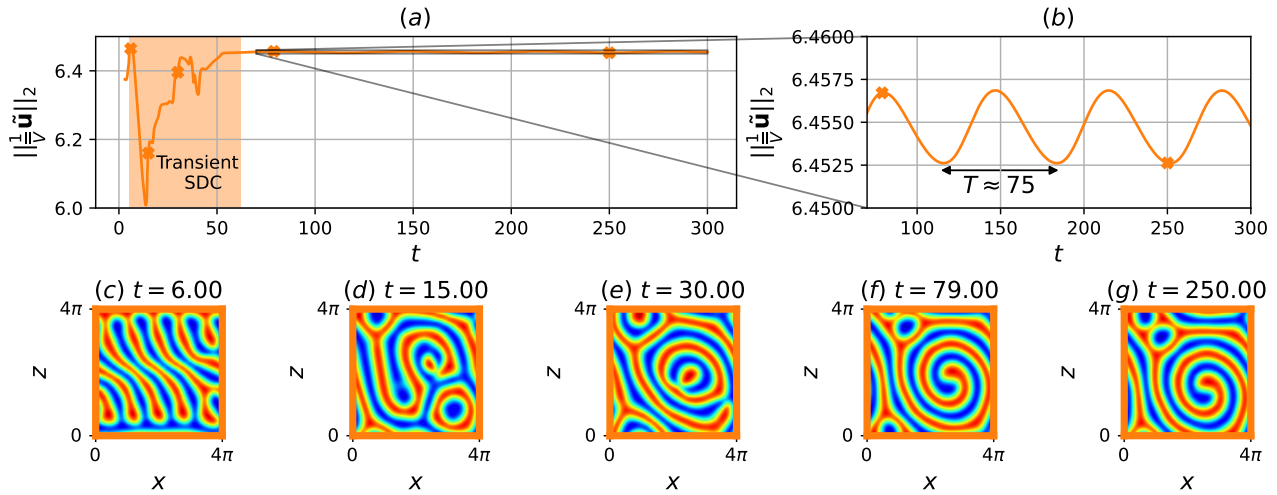


Figure 1.2: (a,b) Time history of the volume ($\bar{V} = L_x L_y L_z$) normalised L2-norm of velocity perturbations from a random initial condition with $\delta = 0.001$ and (c-g) Mid-plane temperature snapshots at $t = 6, 15, 30, 79, 250$. Here, transient chaotic SDC lasts up to $t \approx 70$, before stabilising into an SD state, emerging as a relative periodic orbit with the time period $T \approx 75$ propagating diagonally in the negative x - and z -directions.

& Yin, 2006).

To show whether SDC and elementary states are related, we compare their state space trajectories and the averaged wall-normal temperature profiles. Since the full state space is very high-dimensional, with its dimensionality determined by the number of degrees of freedom dictated by the spatial discretisation scheme, it is therefore very challenging, if not impossible, to visualise the full state space in its entirety. Here, we choose the volume ($\bar{V} = L_x L_z L_y$) normalised L2-norms of velocity ($\|\frac{1}{\bar{V}}\tilde{u}\|_2$) and temperature ($\|\frac{1}{\bar{V}}RaPr\tilde{\theta}\|_2$) perturbations as state space observables, describing the deviation from the conduction state and providing a consistent depiction across different domain sizes, as we shall see later. It is also worth highlighting that the perturbation kinetic/thermal energies are integral quantities and therefore may not distinguish between states that are spatially symmetric or are translations of one another (i.e., ISRs of the same wavenumber that differ in phase). Other integral quantities, such as the Nusselt number, do not provide a clear separation between SDC and ISR. We emphasise that our choice of projection does not capture the full dimensionality of the system, and our intent in using this projection is to provide a qualitative ‘slice’ of its high-dimensional dynamics. As in other studies of turbulent shear flow (see references in §??), low-dimensional projections are commonly used to visualise an otherwise high-dimensional state space. We also note that different choices of projection will naturally change the figures.

Figure 1.3 presents the two chaotic trajectories of SDC from $\Gamma = 16\pi, 8\pi$, four of fourteen transient SDC trajectories obtained and fourteen stable fixed-points of ISRs from $\Gamma = 4\pi$ on a two-dimensional state portrait based on the volume normalised L2-norms of velocity and temperature perturbations. The trajectories begin from $t = 3$, as those for $t < 3$ contain artificial transients and are omitted for clarity. The state space trajectories of SDC ($\Gamma = 16\pi, 8\pi$) and the transient SDC states for $\Gamma = 4\pi$ appear approximately between $(8.4, 6) \lesssim (\|\frac{1}{\bar{V}}\tilde{u}\|_2, \|\frac{1}{\bar{V}}RaPr\tilde{\theta}\|_2) \lesssim (8.7, 6.5)$ shown in figure 1.3(b). This suggests that they are presumably the same type of SDC emerging in different

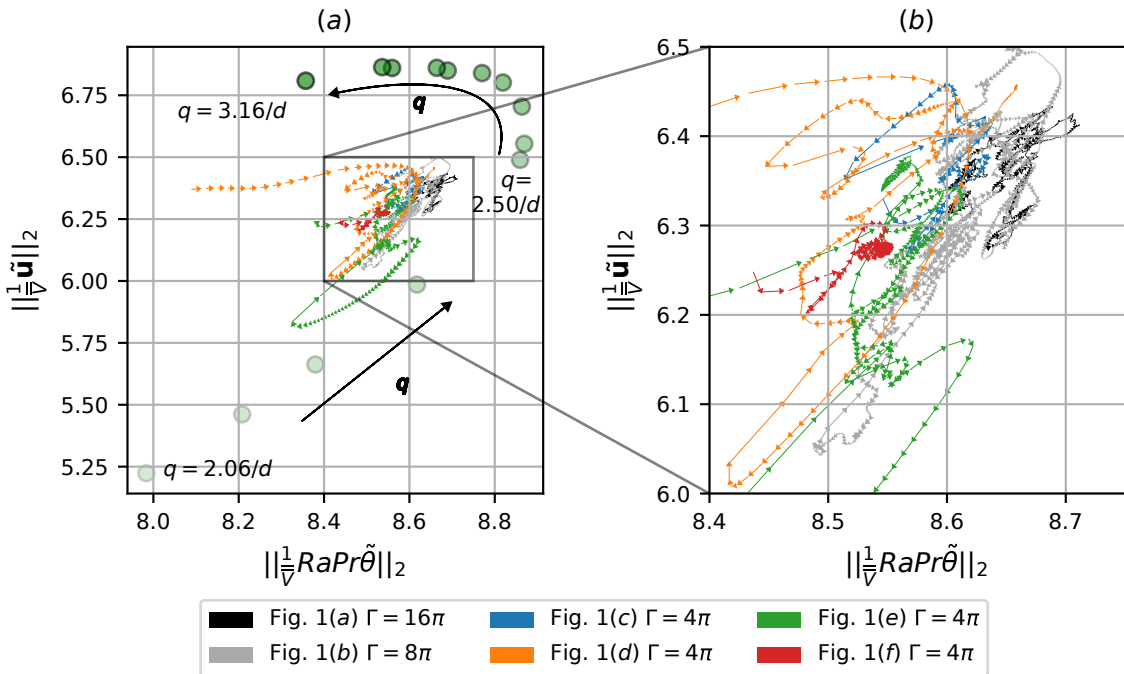


Figure 1.3: (a) State-space portrait in the plane of $\|\frac{1}{V}\tilde{\mathbf{u}}\|_2$ and $\|\frac{1}{V}RaPr\tilde{\theta}\|_2$ for SDC from $\Gamma = 16\pi, 8\pi$ (figures 1.1(a,b)), four transient SDC state proceeding to stable elementary states (figures 1.1(c-f), A.6), and fourteen stable stationary ISRs of wavenumbers $2.0 \leq qd \leq 3.35$. Here, the magnitude of q is denoted by the opacity of the filled symbol (●), increasing from the bottom left and turning toward the top left shown as arrows; (b) Zoomed-in view of (a). The legend refers to the figures for respective trajectories preceding snapshots in figure 1.1.

domains. The closely packed chaotic trajectories are in contrast to the ISRs populating sparsely.

The transient SDC trajectories eventually stabilise into fourteen elementary states in figure 1.4, where the transient SDC trajectories from figure 1.3 are now omitted. Obscured by the transient SDC trajectories initially, the elementary states in figure 1.4 emerge as seven steady states (■), two travelling waves (×), one periodic orbit (dash-dotted line) and four relative periodic orbits (solid line). The SDC trajectories for $\Gamma = 16\pi, 8\pi, 4\pi$ appear near the fourteen elementary states, approximately bounded between $(8.5, 6) \lesssim (\|\frac{1}{V}\tilde{\mathbf{u}}\|_2, \|\frac{1}{V}RaPr\tilde{\theta}\|_2) \lesssim (8.7, 6.5)$ (figure 1.4), in contrast to the larger region occupied by ISRs between $(8, 5.25) \lesssim (\|\frac{1}{V}\tilde{\mathbf{u}}\|_2, \|\frac{1}{V}RaPr\tilde{\theta}\|_2) \lesssim (8.8, 7)$ (figure 1.3(a)). Notably, the state space trajectories of SDC and the elementary states are in close vicinity to the ISR of wavenumbers $q = 2.5/d$ (see figures 1.3), which corroborates with the averaged wavenumber of SDC, $q_{avg} \approx 2.5/d$ (Decker, Pesch, & Weber, 1994; Morris et al., 1993).

The comparison between the time-averaged mean temperature profile, mean-squared temperature fluctuations, and mean-squared velocity fluctuations of SDC (figures 1.1(a,b)) and elementary states (figures 1.1(c-f) and figure A.6) are presented in figure 1.5. In figure 1.5(c), we present the sum of mean-squared x - and z -velocity fluctuations due to horizontal isotropy. The mean temperature profiles of the elementary states closely match those of SDC (figure 1.5(a)). Notably, the mean-squared temperature and velocity fluctuations between SDC states (grey and black dashed curves) of figures 1.5(b-d) are similar. The mean-squared temperature and velocity fluctuations profiles of elementary states are comparable to those of SDC but are, in general, slightly larger in magnitude.

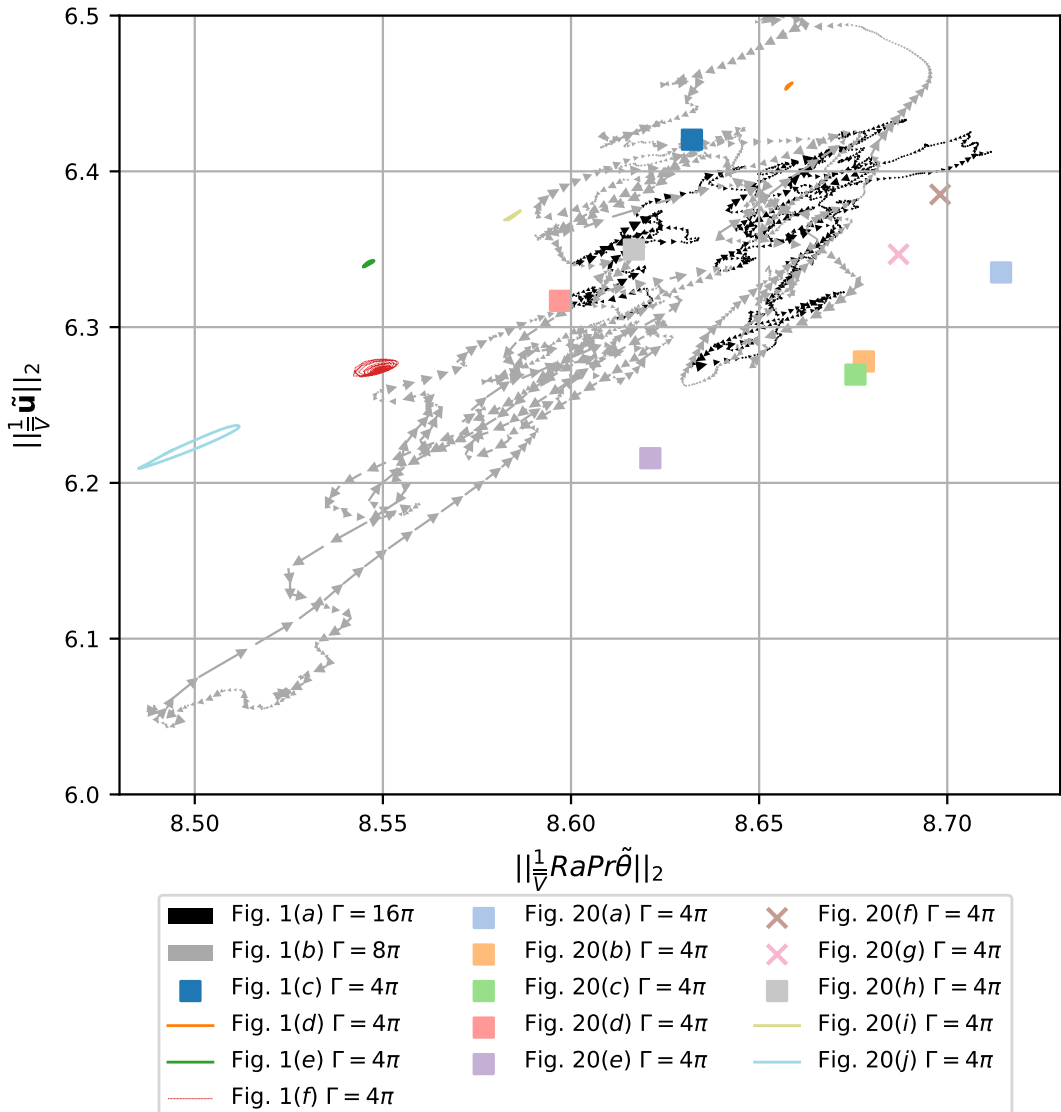


Figure 1.4: State-space portrait (from figure 3) highlighting the transient SDC states for $\Gamma = 4\pi$ proceeding toward stable elementary states (see figures 1.1(c-f), A.6): steady states (■), travelling waves (×), periodic orbit (dash-dotted line) and relative periodic orbits (solid lines).

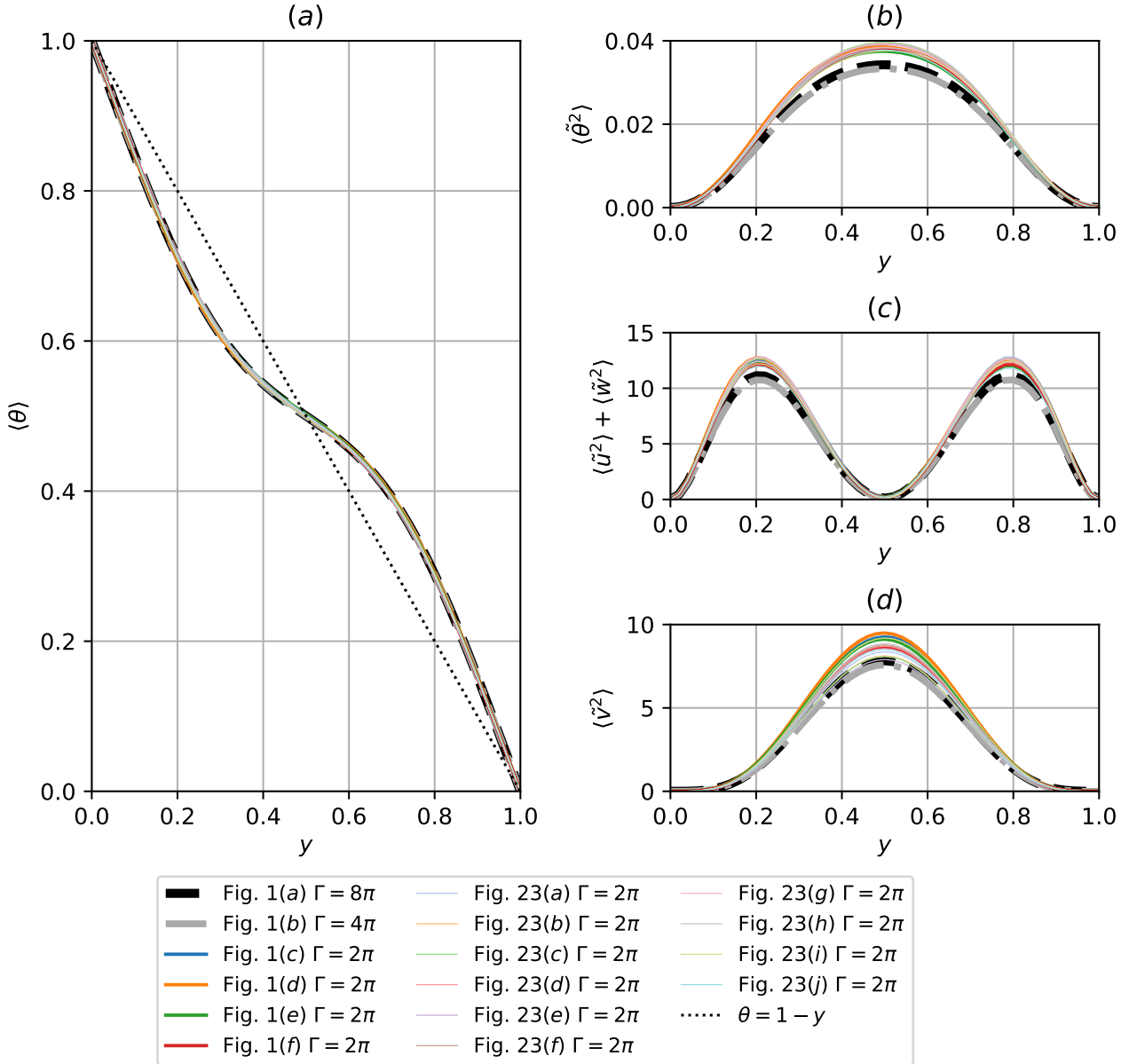


Figure 1.5: Profiles of (a) averaged temperature, (b) root-mean-squared temperature fluctuation, (c) sum of root-mean-squared x - z velocity fluctuations and (d) root-mean-squared wall-normal velocity fluctuations for the SDC and elementary states shown in figures 1.1(a-f) and in Appendix A.5. Note that $\langle \cdot \rangle = \frac{1}{T L_x L_z} \int_{t,x,z} dt dx dz$ refers to the time and plane averaged operator, where T was chosen to be sufficiently long to ensure temporal convergence.

The spatial-temporal complexity of SDC reduces when the domain size is reduced from $\Gamma = 16\pi$ to $\Gamma = 8\pi$, i.e. less disordered spatial features. Reducing the domain from $\Gamma = 8\pi$ to $\Gamma = 4\pi$ led to transient SDC before stabilising into many elementary states. From the conventional view, especially made in the context of shear flow turbulence, this is unexpected as the chaotic state (i.e. turbulence) is commonly described as solution trajectories wandering around unstable invariant solutions (see §??). However, in this particular case observed in RBC, the chaotic state (i.e. SDC) stabilised into stable invariant solutions (elementary states) instead, in contrast to shear flow turbulence where invariant solutions are expected to be unstable. Despite this distinguished feature of the state space, each of the elementary states is still seen to emerge in a spatially localised manner of SDC in an extended domain (figure 1.1), and their spatially-averaged statistics are remarkably similar to those of SDC in extended domains (figure 1.5). Therefore, we consider the elementary states in the minimal domain to be the ‘building blocks’ structure of SDC.

1.4 Multiplicity of edge states

The stable nature of many ISRs and elementary states underpinning SDC implies the existence of state-space boundaries between them (i.e. edge). In this section, we perform the edge tracking between the stable manifolds of ISRs and elementary states to compute the attractors on the edge (i.e. edge states). For the edge tracking, we use the bisection method (see §??), with an initial condition given by

$$\mathbf{s}_0(\mathbf{x}, t=0) = \chi \mathbf{s}_{ISR,q} + (1 - \chi) \mathbf{s}_{elementary}, \quad (1.8)$$

where $\mathbf{s}_0(= [\mathbf{u}_0, \theta_0, p_0]^T)$ refers to an initial condition consisting of a weighted sum, $\chi \in [0, 1]$, between a stable ISR state, $\mathbf{s}_{ISR,q}$ of a wavenumber q , and an elementary state, $\mathbf{s}_{elementary}$ where the subscript refers to its names in figures 1.1(c-f).

Given the large number of stable ISRs and elementary states, we shall focus on the computation of the edge states considering three of the stable ISRs and two of the elementary states. However, in principle, the edge tracking is technically possible with other stable ISRs and elementary states. As such, in general, multiple edge states are expected. The three ISRs are related to three different wavenumbers, denoted by $\mathbf{s}_{ISR,q=2.06/d}$, $\mathbf{s}_{ISR,q=2.24/d}$, $\mathbf{s}_{ISR,q=3.16/d}$ (figures A.7(b,d,j)) respectively, and the two elementary states are SD state, $\mathbf{s}_{spiral-defect}$ (figure 1.1(c)), and PM state, \mathbf{s}_{pacman} (figure 1.1(d)). Using this set of stable ISRs and elementary states, we aim to track the edge near $\mathbf{s}_{ISR,q}$ in the direction of $\mathbf{s}_{elementary}$ by bisecting the initial condition with χ in (1.8), whereby one of the two trajectories across the edge decays toward $\mathbf{s}_{ISR,q}$ and the other is attracted toward transient chaotic state (i.e. SDC), referred to as the ‘lower’ and ‘upper’ trajectories respectively. The bisection of the initial condition is carried out by monitoring the difference in two trajectories with Nu (i.e. ΔNu). When the two trajectories reach a certain time at which $\Delta Nu > 0.0007$, the bisection of the initial condition is repeated using the flow fields from the two different trajectories by replacing $\mathbf{s}_{ISR,q}$ and $\mathbf{s}_{elementary}$ in (1.8) with them. This process is repeated until the edge trajectory reaches an attractor (i.e. an edge state).

$s_{ISR,q}$	$s_{elementary}$	Edge state	State transitioned
$s_{ISR,q}=2.06/d$	$s_{spiral-defect}$	Jagged (Stationary)	Transient Chaos
$s_{ISR,q}=2.06/d$	s_{pacman}	Jagged (Stationary)	Transient Chaos
$s_{ISR,q}=2.24/d$	$s_{spiral-defect}$	Point-defect (Travelling wave)	$s_{bubble-defect}$
$s_{ISR,q}=2.24/d$	s_{pacman}	Forked (Relative Periodic Orbit)	Transient Chaos
$s_{ISR,q}=3.16/d$	$s_{spiral-defect}$	Skewed-varicose (Stationary)	Transient Chaos
$s_{ISR,q}=3.16/d$	s_{pacman}	Skewed-varicose (Stationary)	Transient Chaos

Table 1.1: A summary of the edge states computed. The first two columns denote the pair of initial conditions considered for edge tracking in Eq. (1.8). The names and classification of the edge states are described in the third column. The last column describes the state transitioned from $s_{ISR,q}$ for sufficiently large χ in Eq. (1.8).

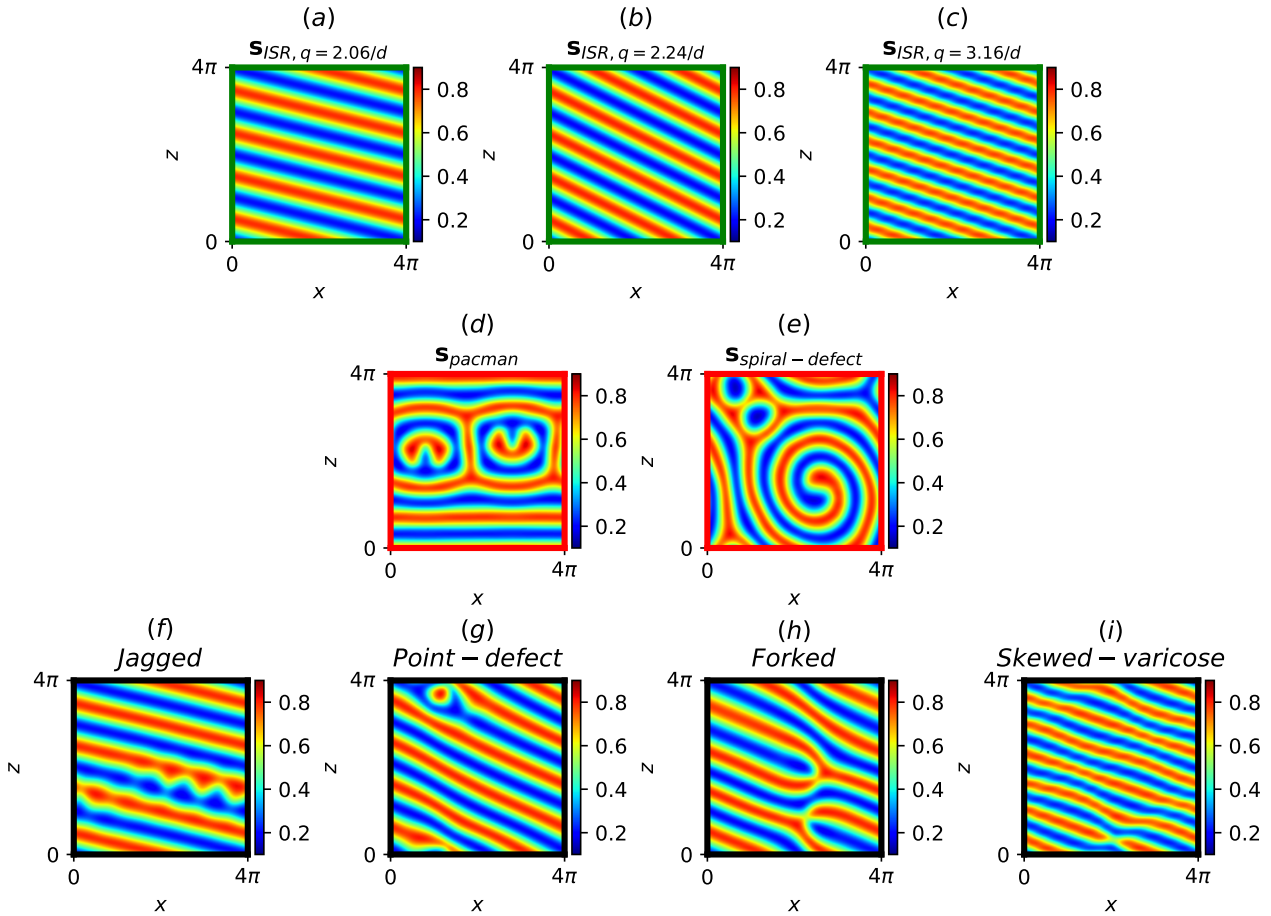


Figure 1.6: Mid-plane temperature fields of ISRs and elementary states used in Eq. (1.8), and the resulting edge states. Here, ISRs (green borders): (a) $s_{ISR,q}=2.06/d$, (b) $s_{ISR,q}=2.24/d$, (c) $s_{ISR,q}=3.16/d$; elementary states: (d) s_{pacman} , (e) $s_{spiral-defect}$; edge states (black borders): (f) *jagged*, (g) *point-defect*, (h) *forked* and (i) *skewed-varicose* edge state.

Table 1.1 summarises the edge states and their dynamical properties computed from six combinations of $s_{ISR,q}$ and $s_{elementary}$ states, and they are visualised with the mid-plane temperature field in figure 1.6. The convection patterns of edge states are often featured with mild spatial complexity compared to SDC and the elementary states. In particular, their patterns contain the underlying convection pattern of $s_{ISR,q}$ with spatially localised defects. We obtained four edge states: specifically, the *jagged* and *skewed-varicose* edge states are stationary, and the *point-defect* and *forked* edge states

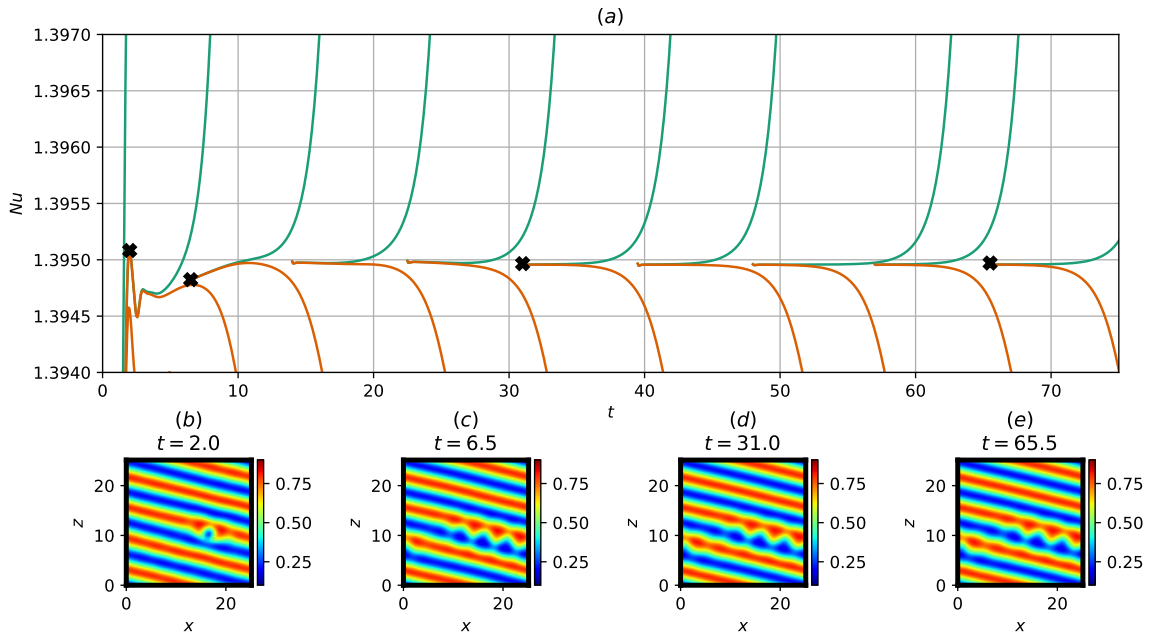


Figure 1.7: (a) Time history of Nu and (b-e) the corresponding mid-plane temperature field snapshots at $t = 2.0, 6.5, 31.0, 65.5$ along the edge trajectory obtained by bisecting $s_{ISR,q=2.06/d}$ and $s_{spiral-defect}$.

are travelling wave and a relative periodic orbit respectively. The *jagged*, *skewed-varicose* and *forked* edge states lie on the boundary, separating the basins of attraction of stable $s_{ISR,q}$ from transient SDC. In the case of the *point-defect* edge state, the solution trajectory is found to bypass the transient SDC state, directly settling into a stable elementary state characterised by bubble-like convection roll defects, $s_{bubble-defect}$. Since the *jagged*, *skewed-varicose*, *forked* edge states are similar in nature, acting as separatrices between $s_{ISR,q}$ states and transient SDC, we will focus our analysis on the *jagged* edge state only, alongside the *point-defect* edge state.

Using Nu as an observable, successive bisections between $s_{ISR,q=2.06/d}$ and $s_{spiral-defect}$ reveal the trajectory along the edge, as illustrated in figure 1.7. The trajectory along the edge spans from $t \approx 0 - 15$, and is initially characterised by a ‘speckled’ defect (figure 1.7(b)). The ‘speckled’ defect grows into a spatially localised jagged-like defect as the trajectory is attracted to the *jagged* stationary edge state from $t \approx 6.5$ onwards (figures 1.7(c-e)). We further examine the two trajectories in the opposite directions along the unstable manifold of the *jagged* edge state in figure 1.8, where the ‘upper’ trajectory evolves into a transient SDC and the ‘lower’ trajectory decays into the original stable $s_{ISR,q=2.06/d}$ state. Starting from the ‘upper’ trajectory (figure 1.8(a)), the spatially localised jagged defect grew in the direction normal to the roll orientation at $t = 80.5$ (figure 1.8(b)), contaminating the adjacent roll structure and propagating through the domain where transient SDC emerges from $t > 80.5$, lasting up to $t \approx 120$ (a snapshot of transient chaotic SDC regime at $t = 90.5$ is shown in figure 1.8(c)). The trajectory subsequently stabilises into a travelling-wave PM elementary state described by ‘pac-man’ like patterns, propagating along the $-x$ direction from $t = 125.5$ to $t = 170.5$ (figures 1.8(d,e)). This is reminiscent of a secondary cross-roll instabilities experienced by low-wavenumber ISRs (such as $s_{ISR,q=2.06/d}$ considered here), where a defect propagates in the direction perpendicular to the rolls (Bodenschatz, Pesch, & Ahlers, 2000). Along the ‘lower’ trajectory (figure

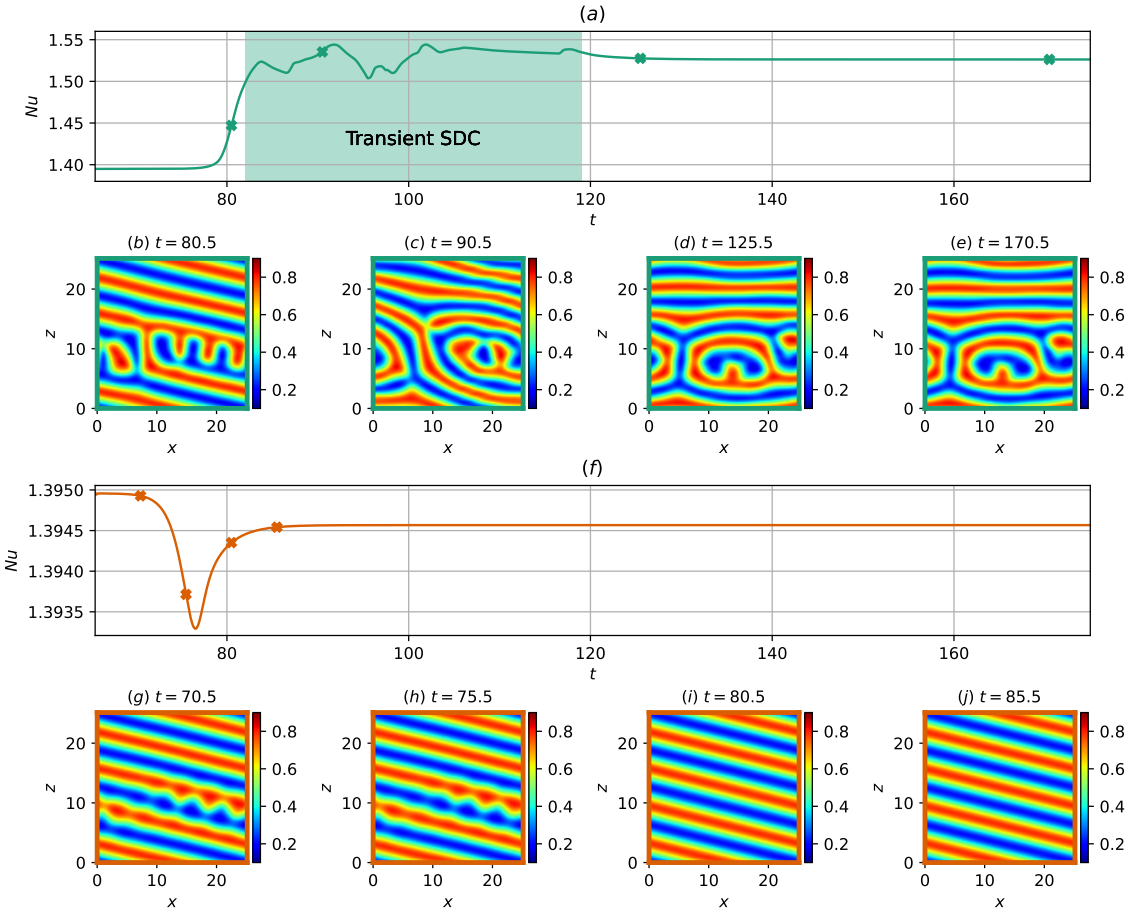


Figure 1.8: Time history of Nu along two opposite directions along the unstable manifold of the *jagged* edge state: (a) ‘upper’ trajectory leading to a transient SDC for $t \approx 85 – 120$ and subsequently to PM state for $t > 120$ and (f) ‘lower’ trajectory stabilising into $s_{ISR,q=2.06/d}$. Mid-plane temperature fields are visualised in (b–e) along the upper trajectory at $t = 80.5, 90.5, 125.5, 170.5$, and in (g–j) along the lower trajectory at $t = 70.5, 75.5, 80.5, 85.5$.

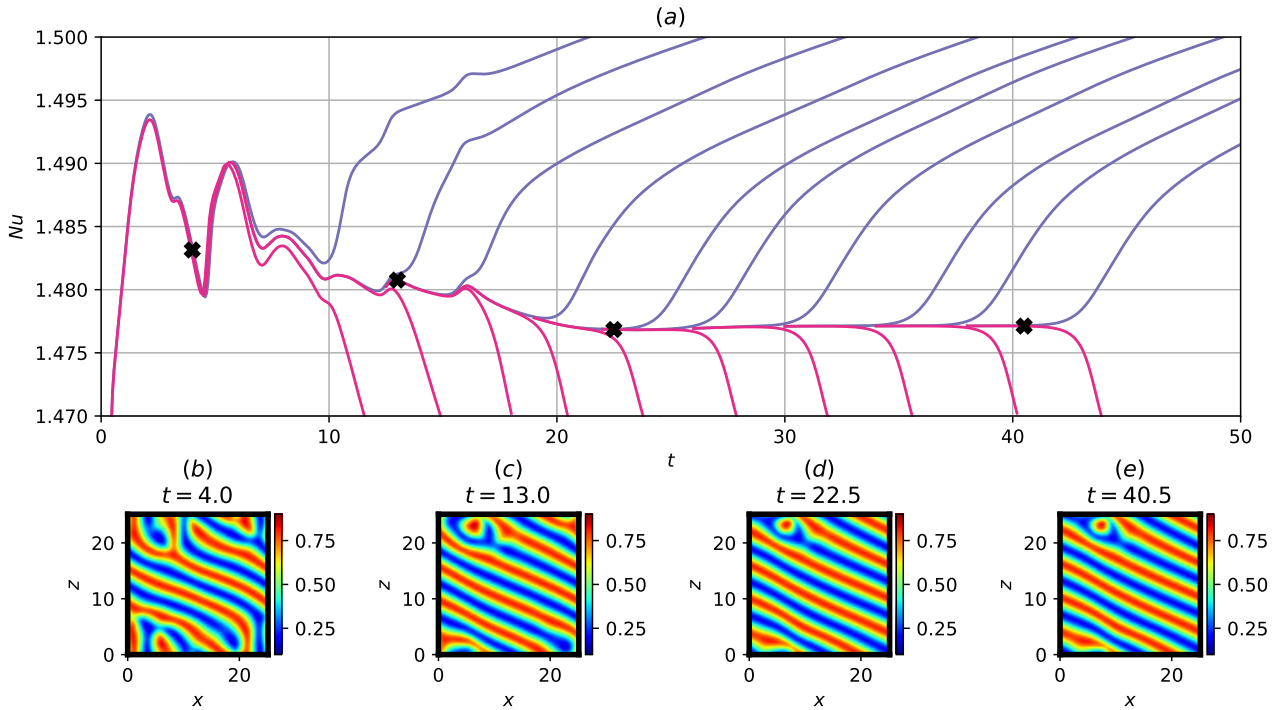


Figure 1.9: a) Time history of Nu and (b-e) the corresponding mid-plane temperature field snapshots at $t = 4, 13, 22.5, 40.5$ along the edge trajectory obtained by bisecting $s_{ISR,q=2.24}$ and $s_{spiral-defect}$.

1.8(f)), the jagged defects diffuses from $t = 70.5$ to $t = 75.5$, decaying into the stable $s_{ISR,q=2.06/d}$ state at $t = 80.5$ (figures 1.8(g-j)).

Next, we analyse the edge trajectory obtained bisecting between $s_{spiral-defect}$ and $s_{ISR,q=2.24}$ in figure 1.9. The trajectory along the edge from $t = 4$ (figure 1.9(b)) is described by time-dependent convection structures. The edge trajectory began to be stabilised into the *point-defect* edge state from $t = 13$ onwards (figure 1.9(c)), propagating along x direction from $t = 22.5$ (figures 1.9(d,e)). It is characterised by the convection structure of the $s_{ISR,q=2.24}$ state with a pointed defect structure, hence referred to as the *point-defect* edge state.

The upper and lower trajectories through two opposite directions of the unstable manifold of the travelling wave *point-defect* edge state are subsequently examined in figure 1.10. Integrating along the upper trajectory (figure 1.10(a)), the spatially localised point-defect structure grew from $t = 43$ to $t = 83$ (figures 1.10(b-d)), saturating into a stationary elementary state at $t = 163$ (figure 1.10(e)) characterised by $s_{ISR,q=2.24}$ with a large bubble defect. Along the lower trajectory (figure 1.10(f)), the spatially localised point defect merged onto the adjacent convection roll from $t = 38$ to $t = 44.5$ (figures 1.10(g,h,i)), stabilising into the $s_{ISR,q=2.24/d}$ state at $t = 53$ (figure 1.10(j)). It is worth noting that, in this particular case, no chaotic transient in the form of SDC has been observed.

Finally, figure 1.11 depicts a state space portrait of stable ISRs, SDC and the edge/elementary states found here. As seen previously, SDC and elementary states are seen to be clustered around the region of $\|\frac{1}{V}\tilde{\mathbf{u}}\|_2 \approx 6.3$ and $\|\frac{1}{V}RaPr\tilde{\theta}\|_2 \approx 8.6$, whereas stable ISRs are distributed along a horseshoe-shaped band (green line). The edge states found in this study are located not far from the (green) horseshoe-shaped band of ISRs, as they presumably lie in a smaller (grey) horseshoe-shape band situated between ISRs and SDC or elementary states. While we have identified four edge states,

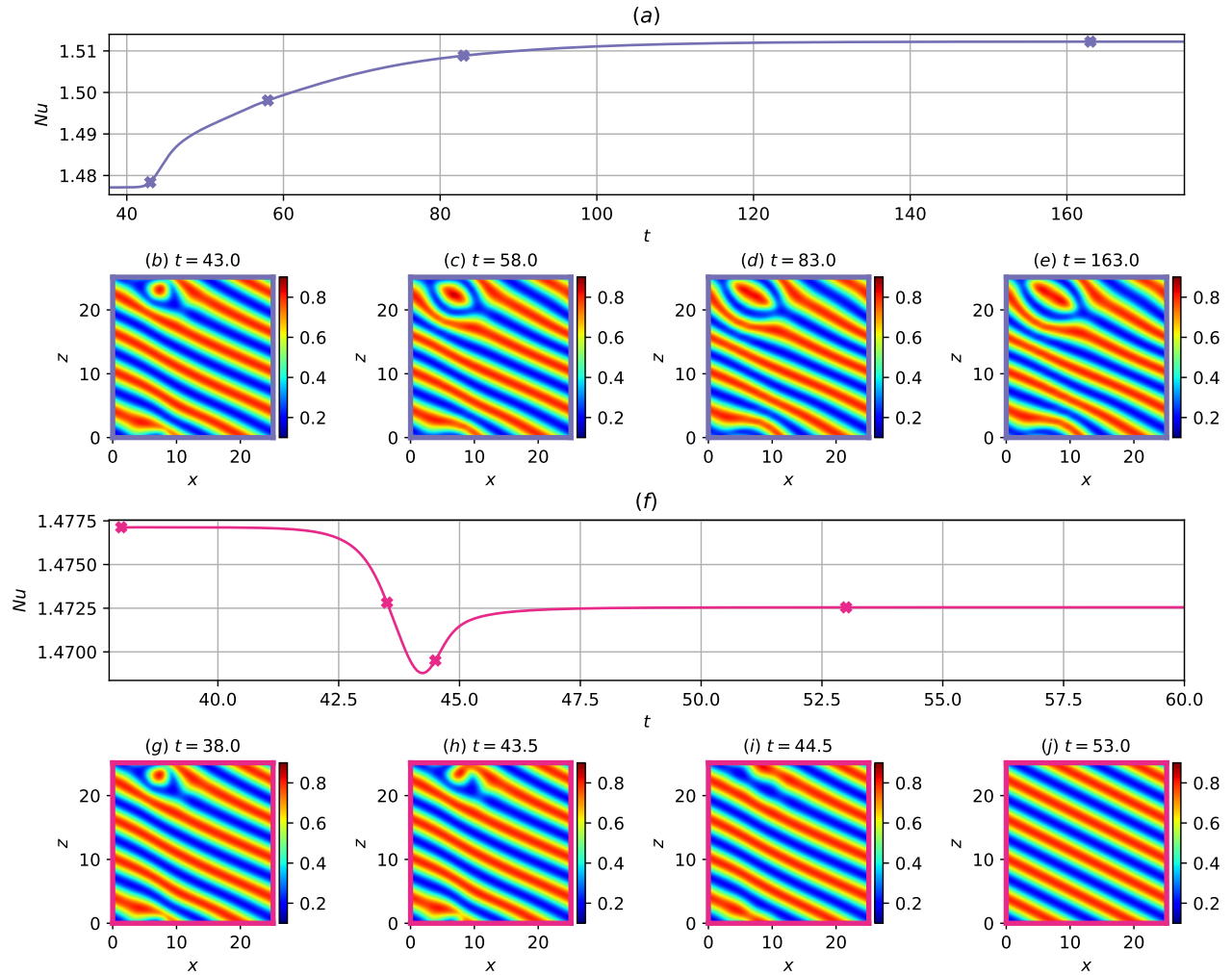


Figure 1.10: Time history of Nu along two opposite directions of the unstable manifold of the *point-defect* edge state: (a) ‘upper’ trajectory leading a stationary elementary state with bubble defect from $t \approx 43 – 163$ and (f) ‘lower’ trajectory decaying to the stable $s_{ISR,q=2.24}$ state. Mid-plane temperature fields are visualised in (b-e) along the upper trajectory at $t = 43.0, 58.0, 83.0, 163.0$, and in (g-j) along the lower trajectory at $t = 38.0, 43.5, 44.5, 53.0$.

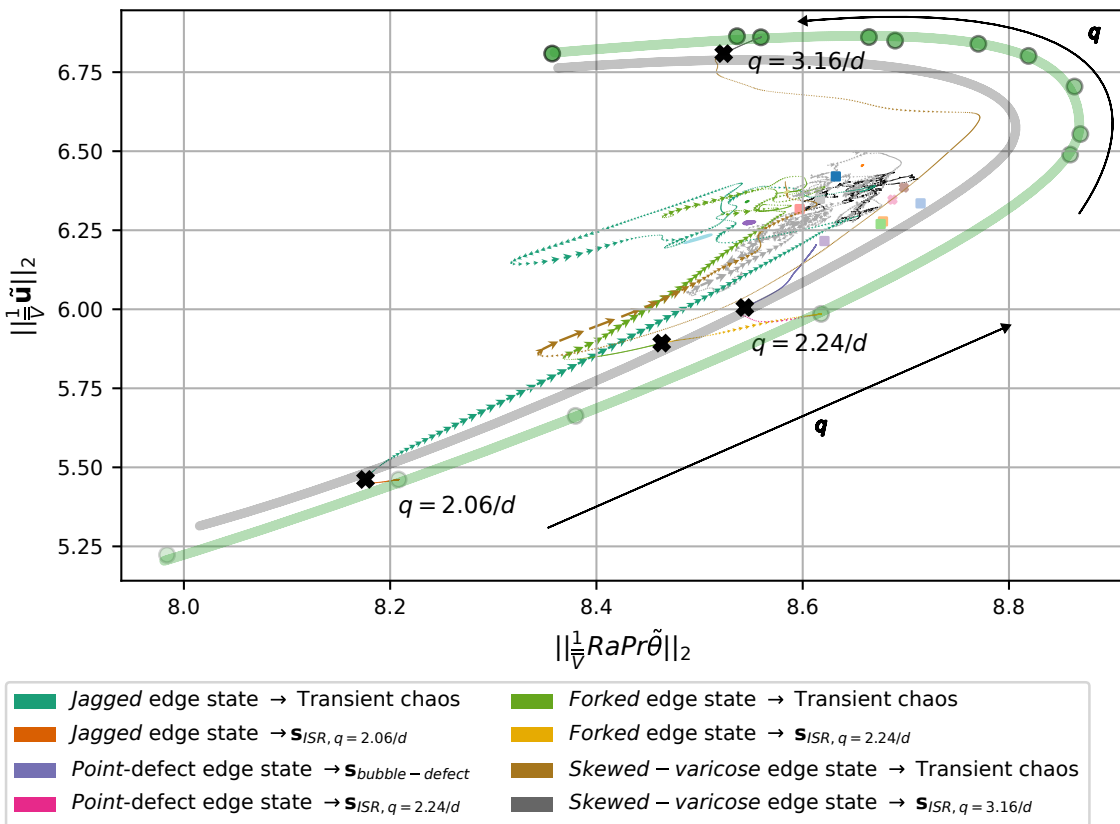


Figure 1.11: Phase portrait of the *jagged*, *point-defect*, *defect* and *skewed-varicose* edge states, along with stable ISRs, elementary states and transient SDC. Green and grey horseshoe lines are the regions, where stable ISRs and edge attractors are expected to be distributed when different sizes of the computational domain are considered.

we expect that there are more edge states, presumably distributed along the (grey) horseshoe-shaped band. It is also worth mentioning that the edge states we found here contain the underlying ISR structure ($s_{q=2.06/d, 2.24/d, 3.16/d}$) modified by spatially localised defects and ‘pinches’ between rolls, supporting its proximity with ISRs in the state space. This feature is also reminiscent of spatially localised edge states identified in boundary layer flows (Khapko et al., 2016). Lastly, we would like to emphasise that we have only considered initial conditions from the states between $s_{ISR,q}$ and $s_{elementary}$ and not strictly between $s_{ISR,q}$ and a transient SDC state. Nevertheless, three of the edge states are found to lie on the boundary separating the stable ISRs from transient SDC, supporting previous findings that the transient chaotic SDC are related to elementary states.

1.5 Unstable ideal straight rolls

Thus far, we have studied the edge and the edge states between some of the stable ISRs and elementary states. The dynamics associated with the unstable ISRs outside of the Busse balloon, however, remain unclear (Busse, 1981). Given that the stable ISRs and SDC form a bistable system, it is expected that some of the unstable ISRs near the Busse balloon would asymptotically reach one of the stable ISRs as the difference between the stable and unstable ISRs would be sufficiently small (Croquette, 1989; Steinberg & Ahlers, n.d.). On the other hand, the unstable ISRs, which exist far from the boundary of the Busse balloon, may well have a sufficiently large deviation from the stable ISRs, implying that they are possibly associated with a state-space route to the SDC. The purpose of this section is to test this hypothesis by examining the long-term behaviour of the linear instabilities of the unstable ISRs.

We consider the linear instabilities of 3 unstable ISRs on the right side of the Busse balloon, with increasing wavenumber of $q = 3.5/d, 4.0/d, 4.5/d$, as shown in figure 1.12(a). The identification of the linear instability mode (or unstable manifold) with the different spanwise wavenumbers β is considered (see (1.6)). Figure 1.12(b) presents the unstable eigenvalues as a function of β . There are 2, 4 and 7 unstable manifolds ($\Re(\lambda) > 0$) for unstable ISRs of $q = 3.5/d, 4.0/d, 4.5/d$ respectively, forming total 13 unstable manifolds. In general, the growth rate and the number of linear instability modes (i.e. the repelling strength and the number of unstable manifolds) increase as q increases. It is worth mentioning that the solutions of unstable ISRs of $s_{ISR,q}(x, y)$ (required for linear stability analysis) are obtained by restricting the computational domain to the 2D $x-y$ plane which artificially suppresses 3D linear instabilities. We also note that the stability analysis of the unstable ISR, $q = 5.0/d$ was not considered as it quickly evolved into an unstable ISR of $q = 3.5/d$, which will be discussed in section §1.5.1.

To consider the long-term behavior in the direction of the unstable manifolds, an initial condition,

$$\mathbf{s}_0(\mathbf{x}, t = 0) = \mathbf{s}_{ISR,q}(\mathbf{x}) + \hat{\mathbf{s}}_\beta(x, y)e^{i\beta z}, \quad (1.9)$$

is prescribed to equation (1.1). Here, $\hat{\mathbf{s}}_\beta e^{i\beta z}$ is the unstable eigenmode, the amplitude of which was scaled such that its total energy (defined in (1.6)) of $\delta = 10^{-5}, 10^{-4}, 10^{-3}$ were considered. The total energy of the eigenmode, $\delta = 10^{-4}$ was found to be sufficiently small enough to ensure linear growth, while large enough to prevent other eigenmodes from being excited. Next, the initial condition is time

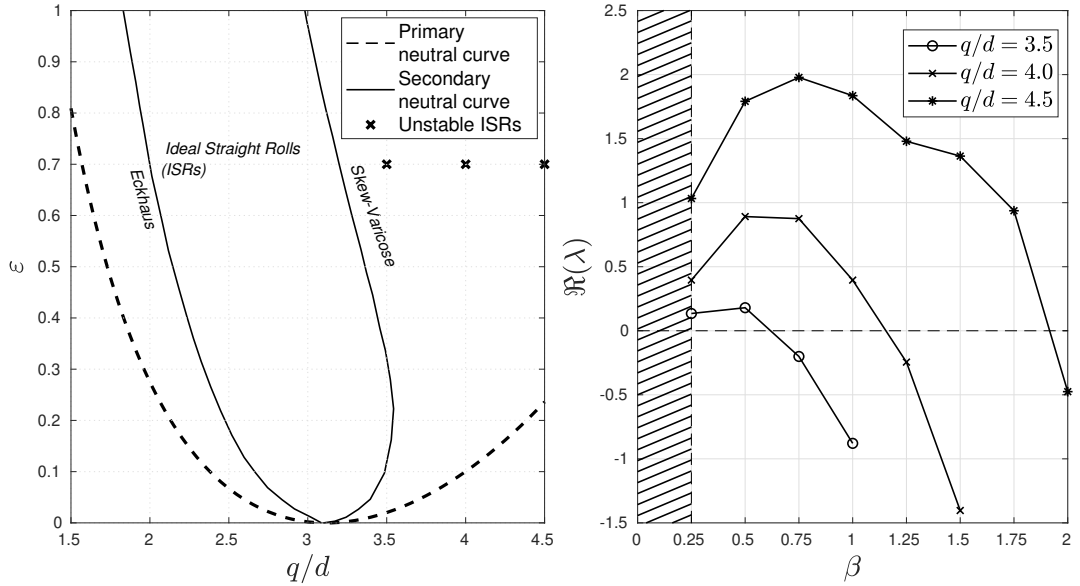


Figure 1.12: (a) Primary and secondary (Busse balloon from figure 1 ([Decker et al., 1994](#))) stability curves and unstable ISRs with $q = 3.5/d, 4.0/d, 4.5/d$; (b) Variation of the growth rate of instabilities of unstable ISRs as a function of spanwise wavenumber β . (Note that there are a total 13 unstable eigenmodes.)

Cases	$\beta = 0.25$	$\beta = 0.50$	$\beta = 0.75$	$\beta = 1.00$	$\beta = 1.25$	$\beta = 1.50$	$\beta = 1.75$
$q = 3.5/d$	ISR _{3.04}	(a) ISR _{2.50}	Stable	Stable	Stable	Stable	Stable
$q = 4.0/d$	ISR _{2.50}	(b) ISR _{3.16}	ISR _{3.00}	ISR _{2.83}	Stable	Stable	Stable
$q = 4.5/d$	ISR _{2.50}	ISR _{2.50}	(c) ISR _{3.00}	ISR _{3.20}	(d) Elementary	ISR _{2.50}	(e) Elementary

Table 1.2: Asymptotic state of secondary linear instabilities of $q = 3.5/d, 4.0/d, 4.5/d$. Subscripts in ISR refer to asymptotic wavenumber q , e.g., ISR_{2.5} refers to ideal straight rolls with wavenumber of $q = 2.5/d$. The asymptotic behaviours of (a-c) and (d,e) are discussed further in §1.5.1 and §1.5.2 respectively.

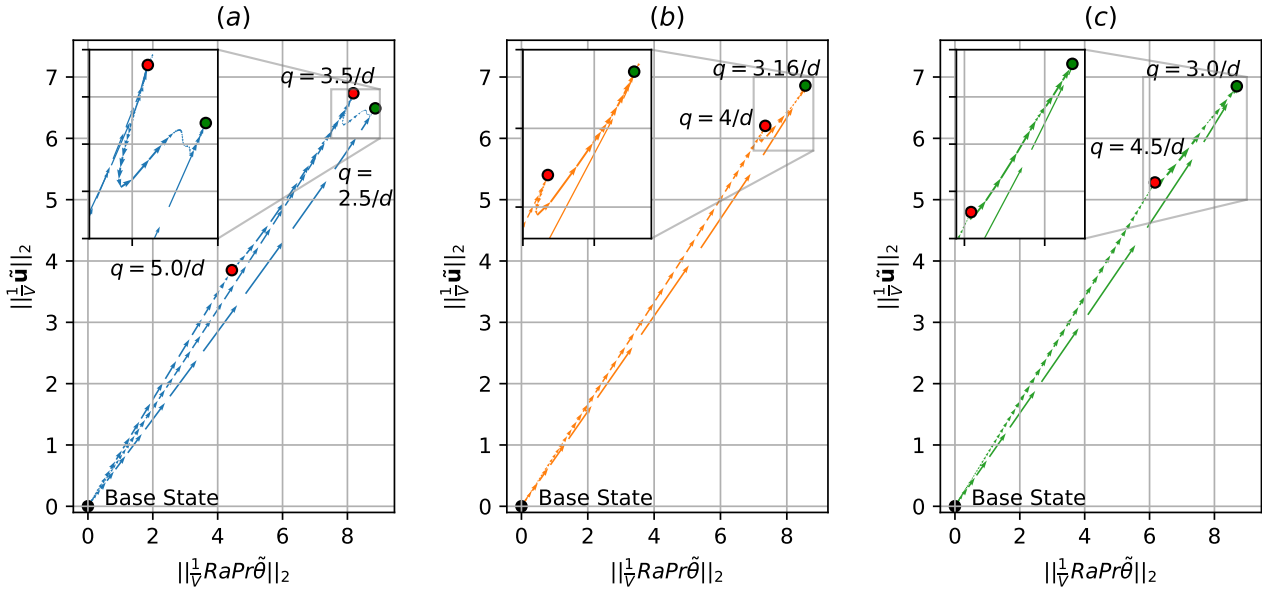


Figure 1.13: The phase-space solution trajectories connecting: (a) unstable base (conductive) state between 10 unstable rolls ($q = 5/d$), 7 unstable rolls ($q = 3.5/d$) and 5 stable rolls ($q = 2.5/d$); (b) unstable base (conductive) state between 8 unstable rolls ($q = 5/d$) and 6 stable rolls ($q = 3.16/d$); (c) unstable base (conductive) state between 9 unstable rolls ($q = 4.5/d$) and 6 stable rolls ($q = 3/d$). Here, the size of the arrows indicates the speed of the solution trajectory (or flow).

integrated over an extended period until an asymptotic state is reached. Table 1.2 shows the asymptotic states of 13 linear instabilities, depicted in figure 1.12(b), of which 11 linear instabilities led to ISRs states, forming a network of heteroclinic orbits which will be discussed in §1.5.1. Only the remaining 2 instabilities led to a transient SDC state before settling into an elementary state discussed further in §1.5.2.

1.5.1 Pathways leading to ISRs - heteroclinic orbits

In this section, the asymptotic behaviour of the most unstable linear modes of ISRs (table 1.2(a-c)) will be discussed. Solution trajectories that connect two invariant states referred to as heteroclinic orbits, are shown in Figure 1.13 which depicts the state space plot of volume normalised L2-norms of velocity and temperature. It reveals a number of heteroclinic orbits, connecting the base state (●), stable (●) and unstable (●) ISRs. Figure 1.13(a) exhibits several solution trajectories linking the base state, stable and unstable ISRs: three orbits connecting the base state to all the stable and unstable ISRs shown, one from the ISR of $q = 3.5/d$ to that of $q = 2.5/d$, and one from the ISR of $q = 5.0/d$ to that of $q = 3.5/d$. Here, caution will need to be taken in interpreting each of the connections as a heteroclinic orbit, because there appears to be an invariant state at which the speed of the solution trajectory nearly vanishes (a sign of the existence of unstable invariant states or ghost states (Strogatz, 2018)): for example, see the solution trajectory between the ISR of $q = 3.5/d$ to that of $q = 2.5/d$ (in the inset of figure 1.13(a)), which will be discussed below with figure 1.14. Starting from the primary base state, the system saturates into an ISR of wavenumber $q = 5.0/d$. Since this ISR is linearly unstable, it evolves into another unstable ISR of $q = 3.5/d$, before ultimately stabilising into

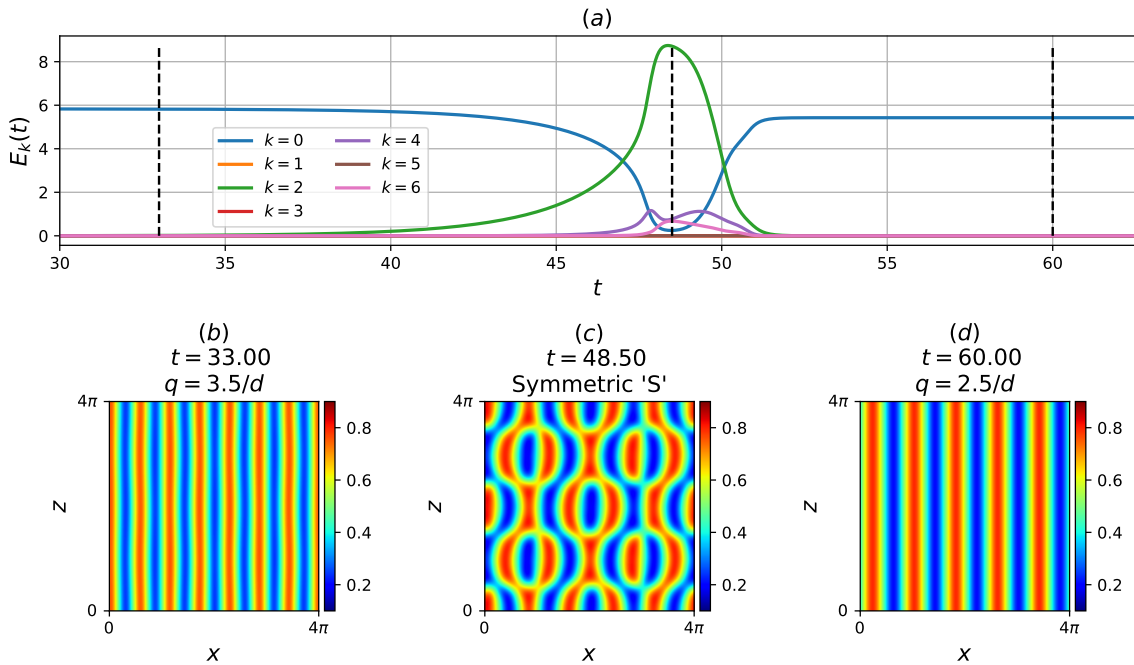


Figure 1.14: Asymptotic behaviour of the linear instability ($\hat{q}_{\beta=0.50}$) about unstable ISR $q = 3.5/d$. (a) Modal energy $E_k(t)$, and temperature snapshots, $\theta(x, z)|_{y=d/2}$ at (b) $t = 33$, (c) $t = 48.5$, (d) $t = 60$.

an ISR of $q = 2.5/d$. Next, figure 1.13(b) shows three solution trajectories connecting the base state, an unstable and stable ISR. Starting from the base state, the system transitions into an unstable ISR of $q = 4/d$ before stabilising into an ISR of $q = 3.16/d$. Lastly, figure 1.13(c) presents three solution trajectories connecting the base state, a stable and unstable ISR. Starting from the base state, it can evolve to an unstable ISR of $q = 4.5/d$ before settling into a stable ISR of $q = 3.0/d$. Figure 1.13 suggests that each of the stable ISRs within the Busse balloon has the basin of attraction, characterised by a web of heteroclinic orbits connecting some of the unstable ISRs outside of the Busse balloon. It is worth emphasising that the connections between the solutions presented here were obtained by time-integrating the dominant unstable manifolds of ISRs. In practice, there are many more unstable manifolds (see table 1.2) which have not been presented, potentially leading to more complex networks of heteroclinic orbits that form the basin of attraction for each stable ISR.

Figure 1.14 describes the asymptotic behaviour with the most unstable eigenmode for $q = 3.5/d$ (table 1.2(a)) in detail, corresponding to the connection between the unstable ISR of $q = 3.5/d$ and the stable ISR of $q = 2.5/d$ in figure 1.13(a). To observe the linear instability defined in Eq. (1.9), we report contribution of modal energy (figure 1.14(a)) as

$$E_k(t) = \frac{1}{2} \int_{\Omega} |\hat{\mathbf{u}}_k(t)|^2 d\Omega, \quad (1.10)$$

where $\hat{\mathbf{u}}_k$ refers to the k -th Fourier coefficient in z -direction. Initially, the simulation starts from the ISR state of 7 rolls ($t = 33$), corresponding to a roll-wavenumber of $q = 3.5/d$. The unstable eigenmode $\hat{s}_{\beta=0.50}$ grows exponentially before peaking at $t = 48.50$, forming an ‘S’-like symmetric state (figure 1.14(c)). Note that, at this point, the time derivative of $E_k(t)$ nearly vanishes, indicating

that the snapshot taken at $t = 48.50$ is potentially close to an unstable invariant state. Finally, the modal energy of $N_z = 2$ decays and the system settles into an ISR state of $q = 2.5/d$ (5 rolls aligned in the x -direction), which is within the Busse balloon. The asymptotic behaviour along the dominant unstable eigenmode for $q = 4.0/d$ and $q = 4.5/d$ is qualitatively similar to figure 1.14, where an unstable ISR stabilises into a stable ISR.

All three cases examined here show that the transition from an unstable ISR to a stable ISR involves an intermediate state, at which $dE_k(t)/dt$ is seen to be relatively small. In the transition pathway from the unstable to stable ISR, it is presumable that there exists an unstable equilibrium (i.e. fixed point/travelling-waves etc.) in the form of the original unstable ISR with its nonlinearly saturated instability, or ghost states (Strogatz, 2018). The existence of such a stationary solution can probably be computed with a typical Newton iteration or variational methods (Parker & Schneider, 2022; Viswanath, 2007), but this is beyond the scope of the present study. In any case, the numerical experiments here suggest that each of the stable ISR has a basin of attraction composed of a network of heteroclinic orbits involving connections between the base state and unstable ISRs.

1.5.2 Pathways leading to elementary states

Now, we discuss the asymptotic behaviour with linear instabilities of $\hat{s}_{\beta=1.75}$ about the unstable ISR of $q = 4.5/d$ (tab 1.2(e)). Contrary to the transitions presented in the previous section, the asymptotic states did not result in ISRs, but transient SDC before settling into an elementary state for case (e) (table 1.2(e))

The asymptotic behavior with $\hat{s}_{\beta=1.75}$ of unstable ISR $q = 4.5/d$ (table 1.2(e)) is presented in figure 1.15. Starting from $t = 1.25$, the unstable ISR state is characterised by 9 convection rolls aligned along the x -axis. The state experiences the linear instability imposed from $t = 1.25$ to $t = 7$, corresponding to an exponential growth in the grey curve ($E_7(t)$ in figure 1.15(a)), marked by cross-convection rolls in figure 1.15(c). Subsequently, the state exhibits a transient SDC behaviour from $t \approx 7$ to $t \approx 80$, characterised by an ‘O’-ring and ‘pac-man’ liked convection pattern illustrated in figure 1.15(d). Following this, the system stabilises into a short-period ($T \approx 1.8$) oscillatory behaviour between $t = 90$ and $t = 110$ (figure 1.15(e)), before transitioning into a long-period time-periodic state from $t = 110$ to $t = 201.75$ (figure 1.15(a) *cont.*), with a period of $T = 51.75$. The convection pattern appears to be travelling diagonally in the negative x - z directions (compare figures 1.15(f,g)), indicating that this state is a relative periodic orbit. Interestingly, the asymptotic behaviour of $\hat{s}_{\beta=1.25}$ about the unstable ISR of $q = 4.5/d$ (table 1.2(d)) also led to an elementary state.

Figure 1.16 presents the state space trajectories of two pathways discussed above, represented by the volume-normalised L2-norms of velocity perturbations, temperature perturbations and Nusselt number. These trajectories are superimposed upon the state space trajectories of SDC and 14 elementary states (figure 1.4). The purple trajectory represents the one along the linear instability direction (i.e. the unstable manifold) of $q = 4.5/d$ with $\beta = 1.25$. Originating from the unstable ISR ($q = 4.5/d$), briefly saturates at $\|\frac{1}{V}\tilde{\mathbf{u}}\| \approx 6.25$ and $\|\frac{1}{V}RaPr\tilde{\theta}\|_2 \approx 8$, before stabilising into a periodic orbit near the *spiral-defect* elementary state (see figure 1.1, represented by the orange trajectory in figure 1.4). The case of $q = 4.5/d$ along the linear instability direction for $\beta = 1.75$ is represented

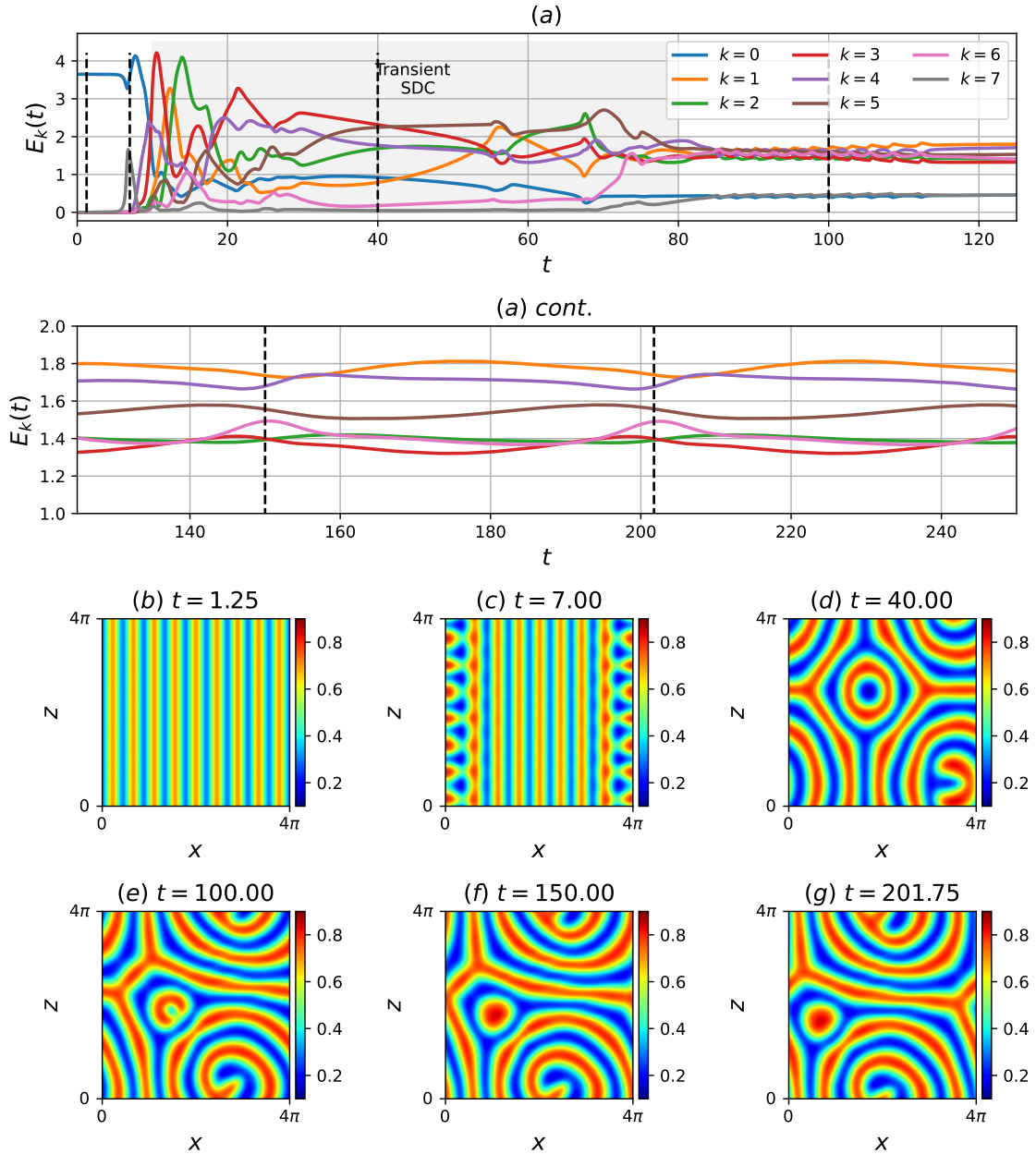


Figure 1.15: Asymptotic behaviour along the linear instability of $\hat{s}_{\beta=1.75}$ about unstable ISR $q = 4.5/d$. (a) Modal energy $E_k(t)$, and temperature snapshots $\theta(x, z)|_{y=d/2}$ at the onset of secondary instability at (b) $t = 1.25$, (c) $t = 7$, following a transient SDC behaviour at (d) $t = 40$, and settling into a elementary state at (e) $t = 100$, (f) $t = 150$ and (g) $t = 201.75$.

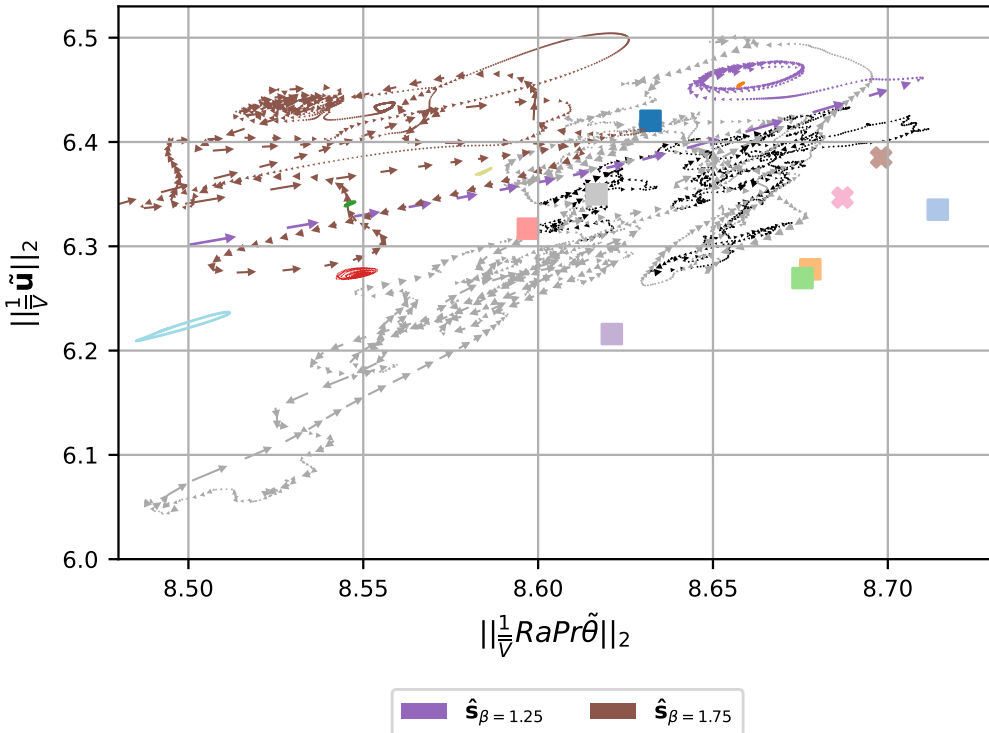


Figure 1.16: State space visualisations using $\|\frac{1}{V}\tilde{u}\|_2$ and $\|\frac{1}{V}RaPr\tilde{\theta}\|_2$, of SDC, and 14 elementary states with colour schemes based upon figure 1.4. The trajectories of two linear instabilities (purple) $\hat{s}_{\beta=1.25}$, (brown) $\hat{s}_{\beta=1.75}$ about an unstable ISR $q = 4.5/d$ leading to elementary states (see figures 1.15) are shown.

by the brown trajectory. Emanating from the unstable ISR ($q = 4.5/d$), the trajectory experiences a period of transient SDC behaviour in the vicinity of elementary states before converging onto a relative periodic orbit, as expected from figure 1.15. It is evident that the two trajectories arising from linear instabilities about the unstable ISR ($q = 4.5/d$) lie within the vicinity of SDC.

1.5.3 A pathway to SDC in an extended domain $\Gamma = 4\pi$

In §1.5.2, we have identified two distinct pathways to elementary states along some unstable manifolds from an unstable ISR. In particular, one of the trajectories evolved into transient SDC before stabilising into an elementary state. This is reminiscent of a chaotic saddle, but with a considerably short lifetime. The transient SDC behaviour observed within the minimal domain implies that if the same initial condition is added in an extended computational domain, it would trigger a chaotic state at least with a longer lifetime. This chaotic state is expected to be SDC in an extended domain, given the analysis in §1.5.2. To examine this hypothesis, we conduct a numerical simulation with an initial condition from the case of table 1.2(e) (i.e. the unstable ISR $q = 4.5/d$ with the instability mode of $\hat{s}_{\beta=1.75}$) in a domain twice larger than each horizontal direction ($\Gamma = 4\pi$).

The solution trajectory along the unstable manifold, $s_{\beta=1.75}$, of ISR $q = 4.5/d$ in an extended domain ($\Gamma = 4\pi$) is presented in figure 1.17. The state, characterised by 18 convection rolls (figure 1.17(b)), experiences the linear instability from $t = 1.25$ to $t = 7$, marked by cross-convection rolls shown in figure 1.17(c). Subsequently, the state exhibits a prolonged period of chaotic behaviour,

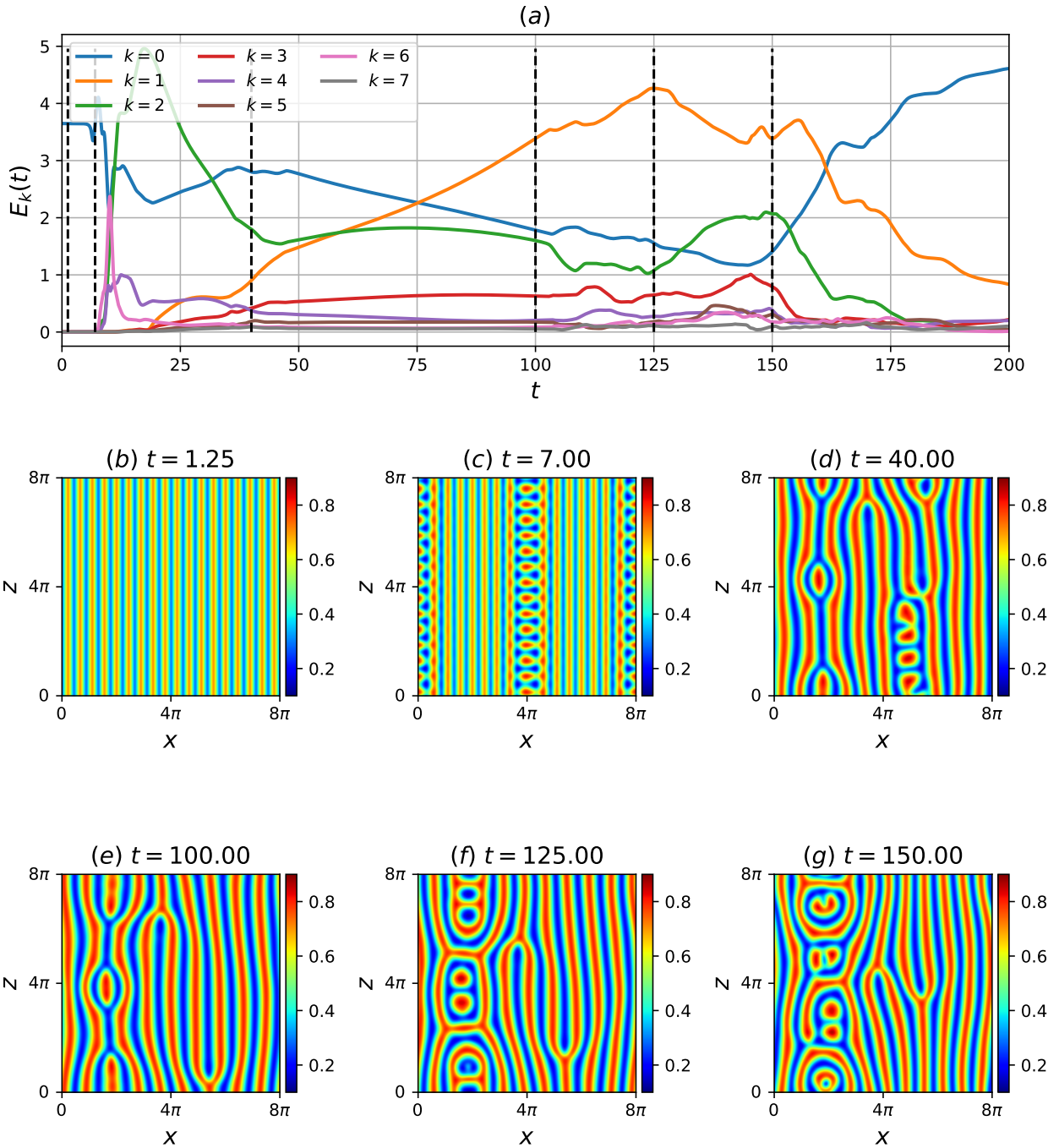


Figure 1.17: Asymptotic behaviour along the linear instability $\hat{s}_{\beta=1.75}$ about unstable ISR $q = 4.50/d$, in an extended domain $\Gamma = 4\pi$. (a) Modal energy $E_k(t)$, and temperature snapshots $\theta(x, z)|_{y=d/2}$, at (b) $t = 1.25$, (c) $t = 7$, (d) $t = 40$, (e) $t = 100$, (f) $t = 125$, (g) $t = 150$.

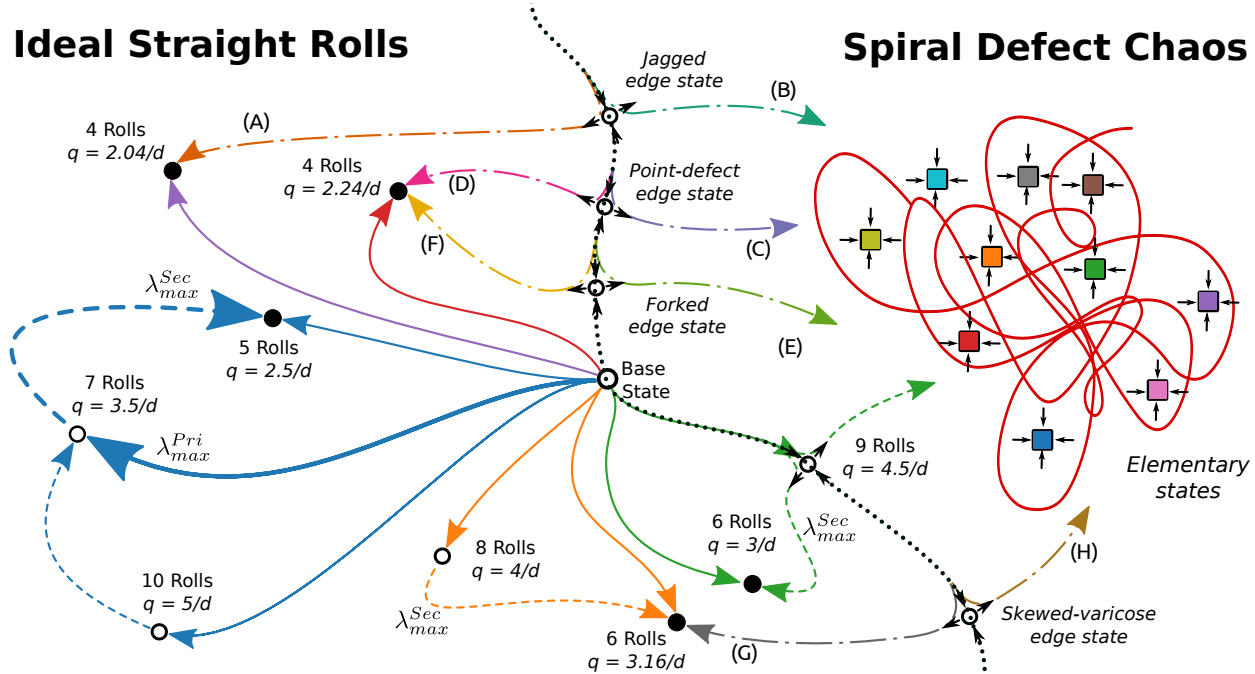


Figure 1.18: State space sketch containing the base, stable and unstable ISRs, edge, elementary states and SDC in a confined domain. Open circles, (\circ) and filled circles/squares (\bullet , \blacksquare) refer to unstable and stable states. Solid ($-$) and dashed lines ($--$) are the solution trajectories along the primary and secondary instabilities respectively, $\lambda_{max}^{Pri,Sec}$ refers to the most unstable primary and secondary linear instability manifolds. Blue, orange and green trajectories denote heteroclinic connections leading toward stable ISRs (trajectories labelled (A-G) and colors adapted from figure 1.13). Dashed-dotted trajectories ($- \cdot -$) refer to solution trajectories emerging from the edge states (color-coded from figure 1.11). The dotted line (\cdots) represents the boundary between ISRs and SDC, consisting of many stable elementary states.

starting from $t = 7$ and lasting beyond $t = 200$. This is in stark contrast to the transient SDC behaviour observed in the minimal domain (figure 1.15), confirming the hypothesis above. Finally, it is interesting to note that the convection patterns of figures 1.17(f,g) contain localised structures that bear resemblance with the stationary *pac-man* (figure 1.1)(c)) and oscillatory *peanut* (figure 1.1(f)) elementary states.

1.6 Summary

Spiral-defect chaos (SDC) has been considered one of the bistable states within a large spatial domain in Rayleigh-Bénard convection. However, existing studies have also shown the presence of multiple stable states in small and large domains, puzzling one's understanding of the bistable system in an extended spatial domain. Starting with numerical simulation in an extended domain ($\Gamma = 16\pi$), we have systematically reduced the computational domain, such that the fundamental patterns of SDC can be isolated.

Through numerical experiments confined within a minimal domain of $\Gamma = 4\pi$, we have identified transient SDC before stabilising in/to stable elementary states of SDC, and 14 different elementary states have been found in this way. From a dynamical system perspective of turbulence in shear

flow, chaotic trajectories (representing turbulence) are typically envisioned to wander among a set of unstable invariant solutions and in some cases, may decay towards the base (laminar) state (see references in §??). Our results for the chaotic trajectories of SDC in a confined spatial domain reveal a distinct scenario, where chaotic trajectories, once tangled into SDC, stabilise into a non-trivial elementary state instead of returning to the base (ISR) state. This finding is new and challenges the understanding of the transition between the conduction state and spiral defect chaos from a dynamical system viewpoint. Despite this, the elementary states are still situated around the chaotic trajectories of SDC in the state space (figure 1.4), and their statistical properties (figure 1.5) and localised spatial structures (figure 1.1) are similar to those of SDC. This suggests that the computed elementary states may serve as spatially local ‘building block’ structures of SDC that interact with each other to form SDC in an extended domain. Within the minimal domain $\Gamma = 4\pi$, we have identified 14 stable elementary states, with a possibility of additional states yet to be found. Notably, the large number of invariant states seem to be characteristic feature of Rayleigh-Bénard fluid systems such as cylindrical RBC ([Borońska & Tuckerman, 2010a, 2010b](#)) and inclined RBC ([Zheng, Tuckerman, & Schneider, 2024a, 2024b](#)).

To further understand the state space structure of SDC, ISRs and possible gateways toward SDC, we furnish a state space sketch of the solution trajectories connecting the base, stable and unstable ISRs, edge, elementary states and SDC, shown in figure 1.18. Starting from the base state, time-integrating along the unstable manifold guided by primary instabilities leads to either stable or unstable ISRs, denoted by solid trajectories. Notably, the most unstable primary instability leads to a 7 roll ISR ($q = 3.5/d$), before saturating into a stable 5 roll ISR ($q = 2.5/d$), following the most unstable secondary instability, depicted by dashed trajectories. These solution trajectories form a network of heteroclinic orbits, connecting the base state with stable ($q = 2.5/d$) and unstable ($q = 3.5/d, 5/d$) ISRs, represented in blue. Further from the boundaries of the Busse balloon, we have identified two more heteroclinic orbits that form a basin of attractor between the base state, and stable, unstable ISRs, labelled as a group of orange and Green trajectories. These heteroclinic orbits are expected in experimental settings where initial conditions and background noise can be controlled precisely. In practice, where precise controls are inaccessible, it is more likely to observe SDC ($\Gamma = 8\pi, 16\pi$) or stable elementary states ($\Gamma = 4\pi$), which are embedded in the chaotic trajectories of SDC (see coloured ■), supporting the notion that SDC is underpinned by elementary states presumably interacting with each other.

We have identified 4 edge states that lie on the boundary between stable ISRs and transient SDC, where the upper and lower trajectories emerging from their unstable manifold are represented by dash-dotted trajectories. Further from the Busse balloon, we have identified an unstable manifold of a 9 roll ($q = 4.5/d$) ISR, leading to the onset of SDC. Consequently, the unstable base state is also expected to lie on the boundary, as a controlled initial condition could guide the system toward the unstable 9-roll ISR, and subsequently the onset of SDC. Finally, the dotted line represents the boundary between ISRs and SDC, consisting of the base state, edge states and unstable 9 roll ISR ($q = 4.5/d$), illustrating four possible routes toward SDC. Although we have considered the unstable manifolds of ISRs for $\Gamma = 4\pi$, we acknowledge that the dimension of such manifolds depends on the

domain size and that the spatially subharmonic instabilities may arise as the domain size increases. Additionally, there may well be other unstable ISRs and edge states along the boundary. However, the investigation into the existence of such states is challenging due to the daunting computational efforts required. Recent advances, such as the framework proposed in ([Schmid, De Pando, & Peake, 2017](#)), may help to accelerate linear stability analysis and facilitate further investigations.

Appendix A

Appendices

A.1 Simulation parameters for Ra - Re sweep

The spectral/ hp quadrilateral element width, heights and polynomial order are kept constant for all simulations, $(\Delta x, \Delta y|_{y=\pm h}, \Delta y|_{y=0}, P) = (0.1\pi, 0.0549, 0.367, 4)$. To resolve the high gradients, the quadrilateral element heights are bunched near the wall, $\Delta y|_{y=\pm h}$, and expanded in the channel center, $\Delta y|_{y=0}$. The basis type employed here consists of the modified Jacobi polynomials, known as the *modified* basis (see §??). Table A.1 describes the number of Fourier expansions, N_z , and temporal resolution of 52 numerical experiments at $Re = 0, 0.1, 1, 10, 100, 500, 750, 1000, 1050, 2000$, and $Ra = 0, 2000, 3000, 5000, 8000, 10000$ with $Pr = 1$ and a large aspect ratio, $\Gamma = 4\pi$. The initial conditions of all numerical experiments were sampled from a statistically stationary solution based on the time history of the Nusselt number and shear. The laminar solution obtained for $Ra = 0$, $Re \leq 1000$ has been omitted in table A.1.

A.2 First- and second-order statistics of the buoyancy- and shear-driven regime

A.2.1 Buoyancy-driven regime

We present the first- and second-order statistics of the buoyancy-dominated regime (shaded in red), consisting of the (1) SDC & ISRs, and (2) ISRs states in figure A.1, illustrating its temporal and plane-averaged streamwise velocity, $\langle w \rangle_{x,z,t}$, temperature, $\langle \theta \rangle_{x,z,t}$, fluctuating wall-normal velocity squared normalised by thermal velocity scale, $\langle \tilde{v}\tilde{v} \rangle_{x,z,t}/u_\kappa^2$, fluctuating temperature squared, $\langle \tilde{\theta}\tilde{\theta} \rangle_{x,z,t}$ and fluctuating span- and streamwise velocities squared normalised by thermal velocity scale, $\langle \tilde{u}\tilde{u} + \tilde{w}\tilde{w} \rangle_{x,z,t}/u_\kappa^2$. We note that the fluctuating components are defined about a temporal-planar averaged quantity, i.e $\tilde{\mathbf{u}} = \mathbf{u} - \langle \mathbf{u} \rangle_{x,z,t}$. The mean temperature profiles (figure A.1(b)), and the fluctuating span- and streamwise velocities (figure A.1(f)) are visually similar for the same Ra , and are nearly independent of Re . However, we observe the dependence on Re at $Ra = 3000$ in the fluctuating temperature squared (figure A.1(d)), and fluctuating wall-normal velocities (figure A.1(c)), likely due to variations in convection structures, particularly in the convection roll wavenumbers. A detailed

Ra	Re	N_z	dt	T	$\frac{d}{\kappa}$
0	1050	64	0.1	8000	-
0	2000	128	0.02	3000	-
2000	0	64	0.05	50	25
2000	0.1	64	0.005	5	25
2000	1	64	0.01	50	25
2000	10	64	0.05	50	2.5
2000	100	64	0.1	50	0.25
2000	500	64	0.1	50	0.05
2000	750	64	0.1	50	0.033
2000	1000	64	0.1	50	0.025
2000	1050	64	0.1	8000	3.81
2000	2000	128	0.02	2800	0.75
3000	0	64	0.05	3000	1500
3000	0.1	64	0.005	300	1500
3000	1	64	0.05	100	50
3000	10	64	0.05	50	2.5
3000	100	64	0.1	10000	50
3000	500	64	0.1	50	0.05
3000	750	64	0.1	50	0.033
3000	1000	64	0.1	50	0.025
3000	1050	64	0.1	8000	3.81
3000	2000	128	0.02	2800	0.75
5000	0	64	0.005	1200	600
5000	0.1	64	0.001	800	4000
5000	1	64	0.01	2500	1250
5000	10	64	0.05	500	25
5000	100	64	0.1	1000	5
5000	500	64	0.05	8000	8
5000	750	64	0.05	8000	5.33
5000	1000	64	0.02	8000	4
5000	1050	64	0.02	8000	3.81
5000	2000	128	0.02	2800	0.75
8000	0	64	0.0025	600	300
8000	0.1	64	0.0005	600	3000
8000	1	64	0.005	600	300
8000	10	64	0.05	500	25
8000	100	64	0.1	5000	25
8000	500	64	0.05	10000	10
8000	750	64	0.05	8000	5.33
8000	1000	64	0.02	8000	4
8000	1050	64	0.02	8000	3.81
8000	2000	128	0.02	2800	0.75
10000	0	64	0.0025	1000	500
10000	0.1	64	0.00025	800	4000
10000	1	64	0.0025	600	300
10000	10	64	0.05	12000	600
10000	100	64	0.1	8000	40
10000	500	64	0.05	8000	8
10000	750	64	0.05	8000	5.33
10000	1000	64	0.02	8000	4
10000	1050	64	0.02	8000	3.81
10000	2000	128	0.02	2800	0.75

Table A.1: The summary of the spatial and temporal resolution for a given Re , Ra . N_z denotes the number of Fourier expansions in the z -direction. $dt, T, d/\kappa$ denotes the timestep, final time and the final time scaled by the thermal timescale.

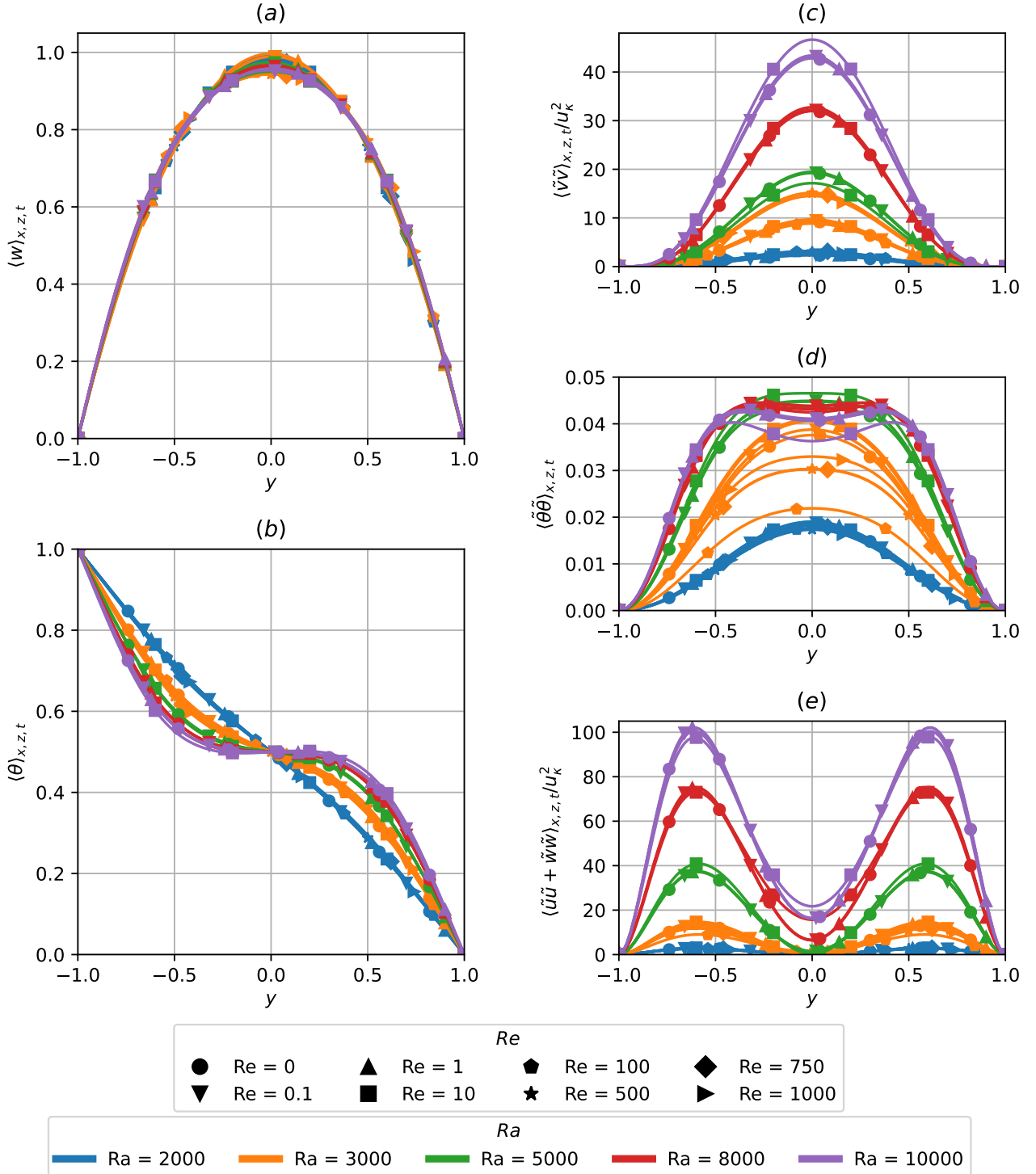


Figure A.1: The wall-normal distribution of temporal and plane- averaged (a) streamwise velocity, (b) temperature, (c) fluctuating wall-normal velocity squared normalised by thermal velocity scale, (d) fluctuating temperature squared and (e) fluctuating span- and streamwise velocities squared normalised by thermal velocity scale of buoyancy-driven regime shaded in red in figure ??.

analysis of how the statistical properties vary with roll wavenumber is beyond the scope of this work. We propose that the underlying flow structure, consisting of convection rolls, describes the buoyancy-driven regime, shaded in red in figure ???. In this regime, the strength of the convection is primarily controlled by Ra , akin to RBC, and remains independent of Re .

A.2.2 Shear-driven regime

As Re falls within the range of $1050 \leq Re \leq 2000$, shear-driven turbulence dominates, where the impact of Ra on the first- and second-order statistics is weakly dependent on Ra in figure A.2. Figure A.2 describes the temporal and plane-averaged streamwise velocity, $\langle w \rangle_{x,z,t}$, temperature, $\langle \theta \rangle_{x,z,t}$, fluctuating streamwise velocity squared, $\langle \tilde{w}\tilde{w} \rangle_{x,z,t}$, fluctuating wall-normal velocity squared, $\langle \tilde{v}\tilde{v} \rangle_{x,z,t}$, fluctuating spanwise velocities squared, $\langle \tilde{u}\tilde{u} \rangle_{x,z,t}$, fluctuating Reynolds stresses $\langle \tilde{v}\tilde{w} \rangle_{x,z,t}$, and fluctuating temperature squared, $\langle \tilde{\theta}\tilde{\theta} \rangle_{x,z,t}$ at $Re = 2000, 1050$ for $Ra \in [0, 10000]$. The flow structures appear as uniform, featureless turbulence (Tuckerman, Kreilos, Schröbsdorff, Schneider, & Gibson, 2014) at $Re = 2000$, independent of Ra . The spacetime figure of near-wall ($y^+ = 15$), wall-normal and spanwise perturbation kinetic energy, $\mathcal{E}_{u'+v'}$, at $Re = 2000$, $t \in [0, 2800]$, illustrating spatially uniform featureless turbulence, visually distinguishable within $Ra \in [0, 10000]$, corroborating with their Ra -independent first- and second-order statistics in figure A.2. In other words, the dominant physical mechanism is shear-driven turbulence at $Re = 2000$, independent of Ra .

As Re approaches $Re = 1050$, the midplane temperature in figure ?? shows regions of spatially localised structures, indicating the presence of turbulent-laminar bands, described in figure ?? and ?? later. The mean streamwise velocity and temperature gradients at both ends of the wall, and second-order statistics, are enhanced slightly from $Ra = 0$ to $Ra = 10000$. This enhancement could be due to the coexistence of longitudinal rolls with turbulent bands at $Ra = 10000$, discussed in §???. Notably, we have also included the statistics for a subcritical case ($Ra < Ra_{\parallel}$) at $Ra = 1000$, indicating the presence of subcritical effects as the statistics are slightly enhanced from $Ra = 0$ to $Ra = 1000$, reported by John Soundar Jerome, Chomaz, and Huerre (2012). Nonetheless, there is a distinct change of state between $Re = 1000$ to 1050 (see figure ??), marked by the transition from the longitudinal/intermittent roll regime to shear-driven turbulence at $Re \geq 1050$, thus, shaded in blue in figure ??.

A.3 Growth rates of primary instabilities

Figure A.4 shows the eigenvalues of the primary instabilities as a function of its spanwise wavenumber αd , leading to the onset of longitudinal rolls at $Re = 1050$. The results are obtained using a Chebyshev-collocation method discretised by 51 Chebyshev polynomials (Driscoll, Hale, & Trefethen, 2014). The crosses denote the spanwise wavenumbers admissible within the domain $\Gamma = \pi/2$, where $\alpha d = 4$ corresponds to the dominant eigenmode.

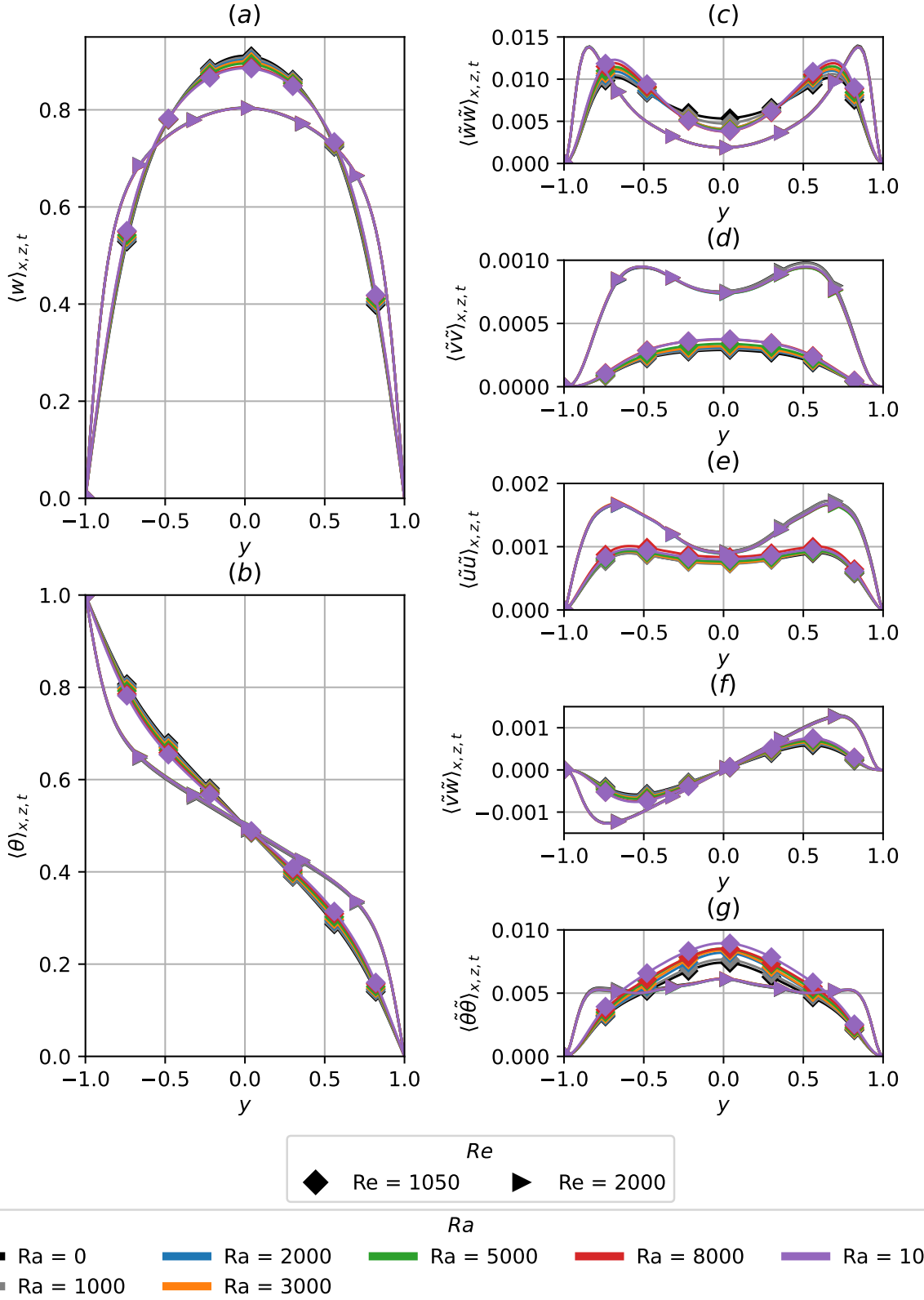


Figure A.2: The wall-normal distribution of temporal and plane- averaged (a) streamwise velocity, (b) temperature, (c) fluctuating streamwise velocity squared, (d) fluctuating wall-normal velocity squared, (e) fluctuating spanwise velocities squared, (f) fluctuating Reynolds stresses and (g) fluctuating temperature squared in the shear-driven regime shaded in blue in figure ??.

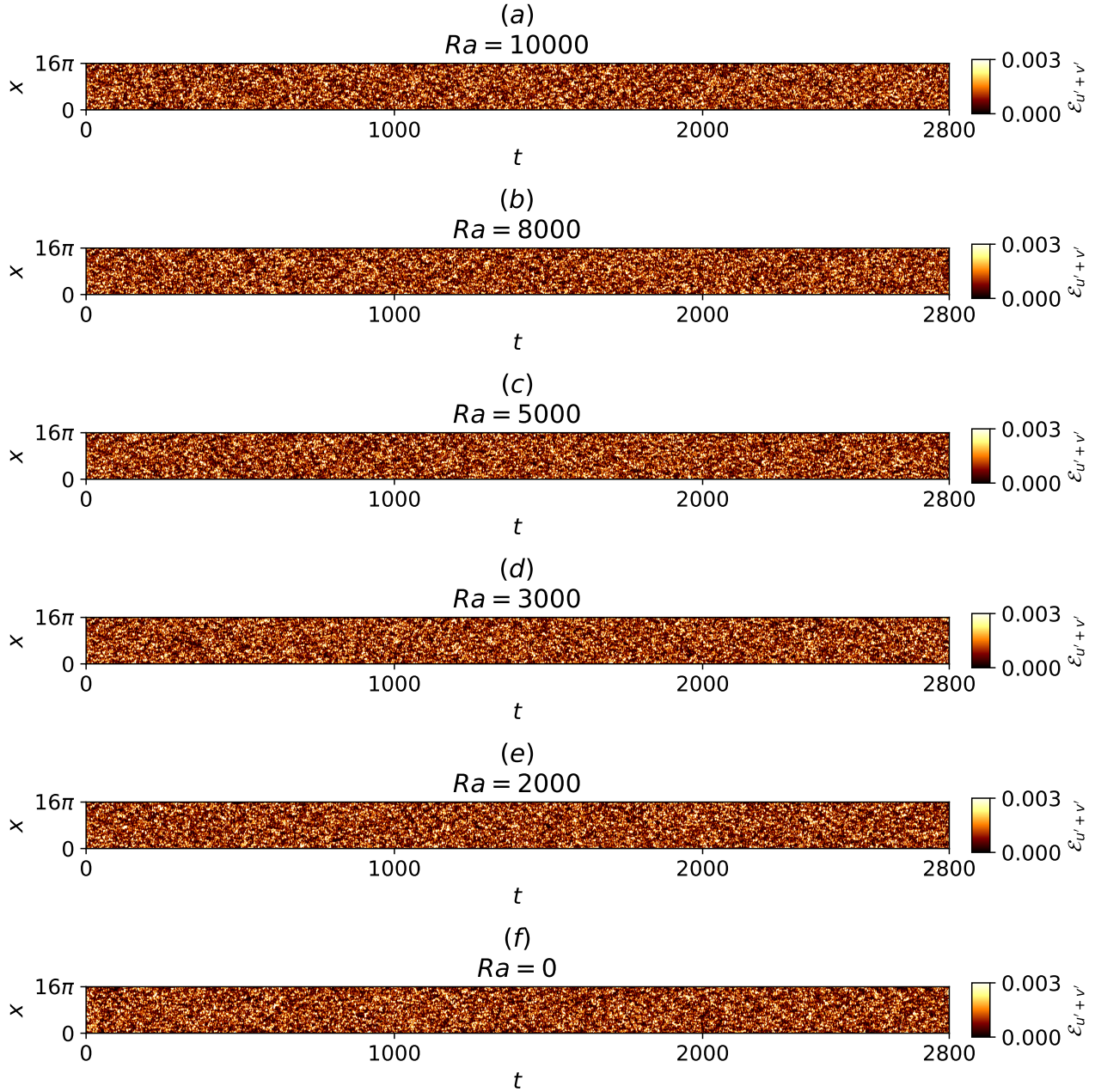


Figure A.3: Spacetime plots of near-wall, wall-normal and spanwise perturbation kinetic energy for $Re = 2000$, $t \in [0, 2800]$, $\Gamma = 4\pi$ at (a) $Ra = 10000$, (b) $Ra = 8000$, (c) $Ra = 5000$, (d) $Ra = 3000$, (e) $Ra = 2000$, (f) $Ra = 0$.

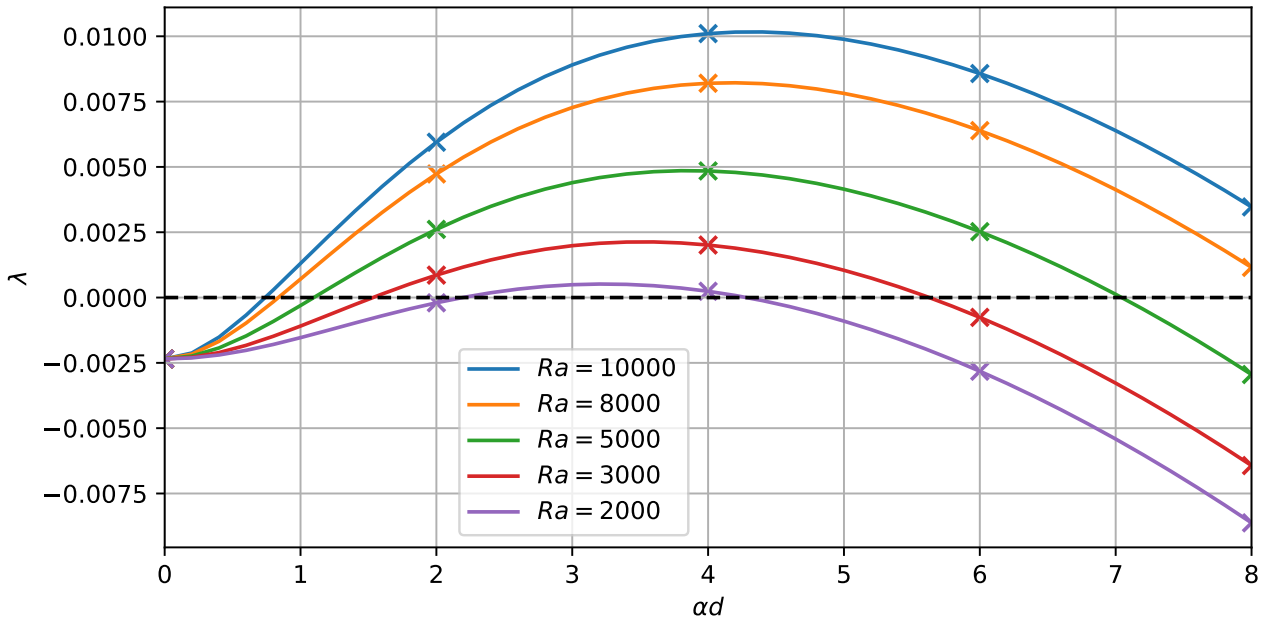


Figure A.4: Growth rates of primary instabilities at $Ra = 10000, 8000, 5000, 3000, 2000$ leading to the onset of longitudinal rolls against spanwise wavenumber of αd at $Re = 1050$.

A.4 Verification of linear stability analysis

Figure A.5 shows the eigenvalues as a function of spanwise wavenumber β of RBC at $\varepsilon = 0.7$. The results are obtained using Nektar++ and compared against a Chebyshev-collocation method discretised by 101 Chebyshev polynomials Driscoll et al. (2014).

A.5 Other elementary states and ISRs

Figure A.6 presents snapshots of temperature slices ($\theta(x, z)|_{d/2}$), depicting ten distinct elementary states. These states are obtained within a minimal domain $\Gamma = 2\pi$, consisting of eight stationary states (figures A.6(a-h)) and two travelling-wave states (figures A.6(i,j)). Figure A.7 features a snapshot of fourteen ideal straight rolls (ISRs), and they satisfy rotational symmetry about the y -axis and mirror symmetries about the x - and z -axes due to the horizontal isotropy of the present system. These ISRs represent stable fixed-points in the state space of figures 1.3, 1.4, 1.11, 1.16.

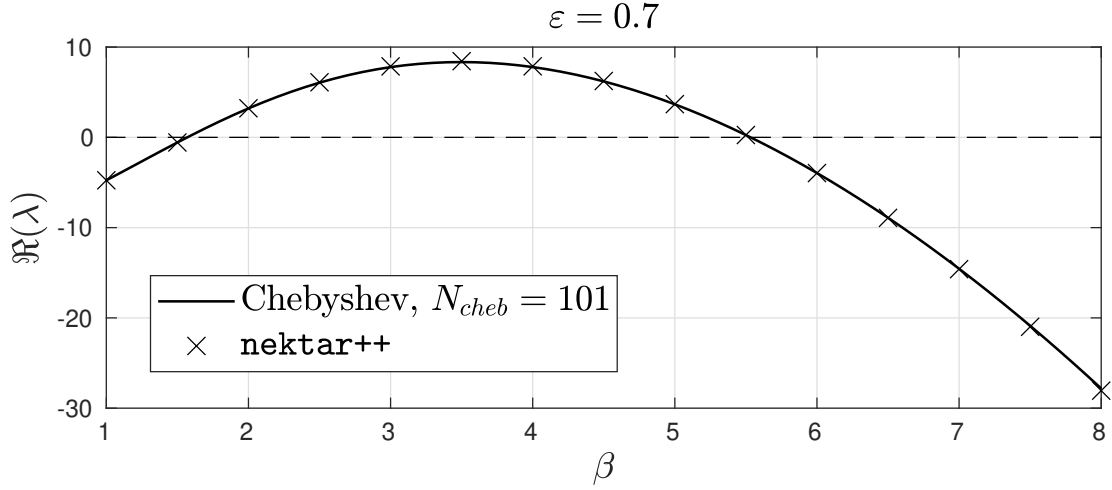


Figure A.5: Eigenvalues of primary instabilities of RBC at $\varepsilon = 0.7$ computed in Nektar++ compared against a Chebyshev-collocation method with 101 Chebyshev expansions.

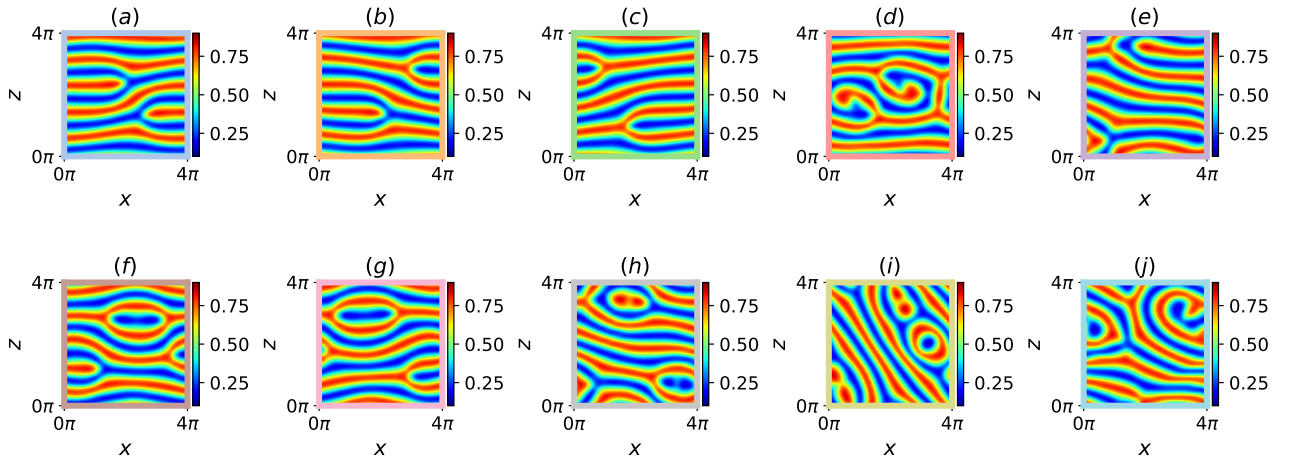


Figure A.6: Temperature snapshots, $\theta(x, z)|_{y=d/2}$, of 10 elementary states confined within a minimal domain $\Gamma = 2\pi$: (a) steady ‘forked-A’ state, (b) steady ‘forked-B’ state, (c) steady ‘forked-c’ state, (d) steady ‘twin-armed’ state, (e) steady ‘tri-rolls’ state, (f) travelling-wave ‘O-a’ state, (g) travelling-wave ‘O-b’ state, (h) steady ‘keyhole’ state, (i) relative periodic orbit ‘eye’ state, (j) relative periodic orbit ‘S’ state

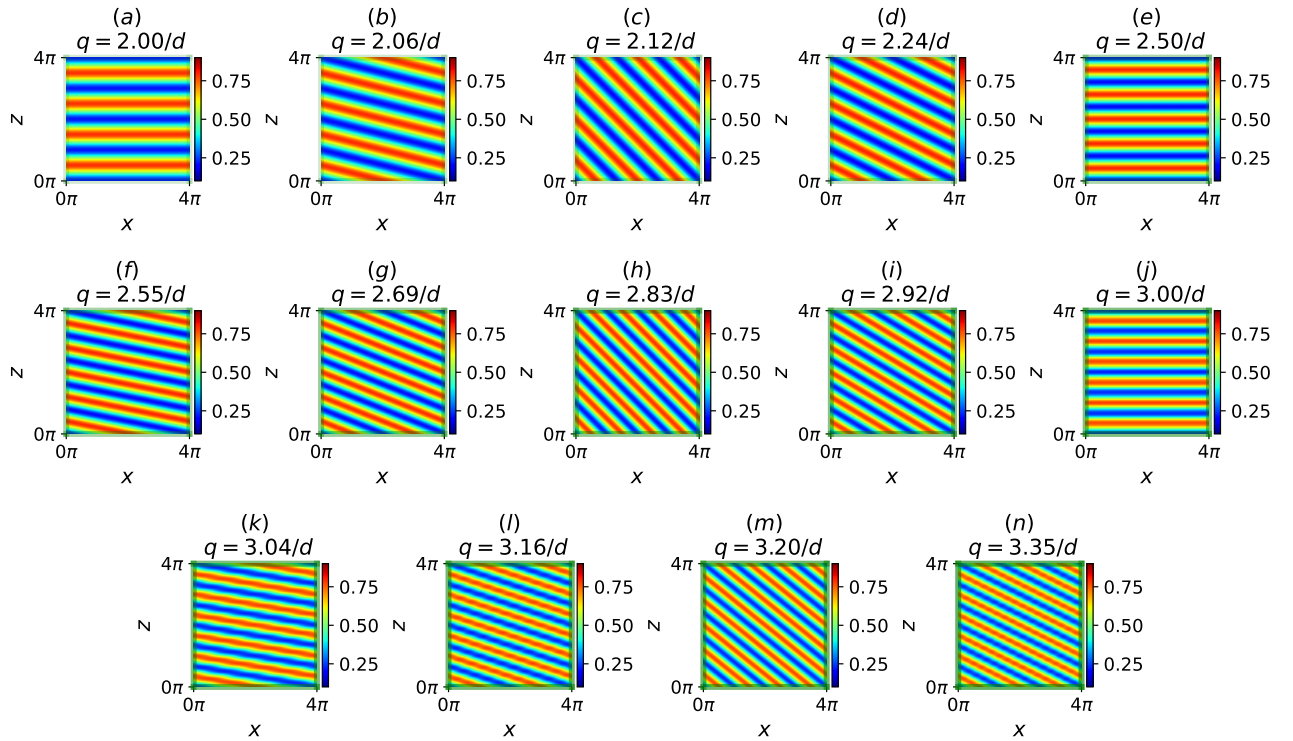


Figure A.7: Temperature snapshots, $\theta(x, z)|_{y=d/2}$, of 14 stable ideal straight rolls (ISRs) confined within a minimal domain, $\Gamma = 6.28$. Plots (a-n) are ordered in increasing wavenumbers, $q \in (2/d, 3.35/d)$.

References

- Bodenschatz, E., Pesch, W., & Ahlers, G. (2000, January). Recent Developments in Rayleigh-Bénard Convection. *Annual Review of Fluid Mechanics*, 32(1), 709–778. Retrieved 2025-03-25, from <https://www.annualreviews.org/doi/10.1146/annurev.fluid.32.1.709> doi: 10.1146/annurev.fluid.32.1.709
- Borońska, K., & Tuckerman, L. S. (2010a, March). Extreme multiplicity in cylindrical Rayleigh-Bénard convection. II. Bifurcation diagram and symmetry classification. *Physical Review E*, 81(3), 036321. Retrieved 2025-03-25, from <https://link.aps.org/doi/10.1103/PhysRevE.81.036321> doi: 10.1103/PhysRevE.81.036321
- Borońska, K., & Tuckerman, L. S. (2010b, March). Extreme multiplicity in cylindrical Rayleigh-Bénard convection. I. Time dependence and oscillations. *Physical Review E*, 81(3), 036320. Retrieved 2025-03-25, from <https://link.aps.org/doi/10.1103/PhysRevE.81.036320> doi: 10.1103/PhysRevE.81.036320
- Busse, F. H. (1981). Transition to turbulence in Rayleigh-Beénard convection. In H. L. Swinney & J. P. Gollub (Eds.), *Hydrodynamic Instabilities and the Transition to Turbulence* (Vol. 45, pp. 97–137). Berlin, Heidelberg: Springer Berlin Heidelberg. Retrieved 2025-05-29, from http://link.springer.com/10.1007/3-540-13319-4_15 (Series Title: Topics in Applied Physics) doi: 10.1007/3-540-13319-4_15
- Cakmur, R. V., Egolf, D. A., Plapp, B. B., & Bodenschatz, E. (1997, September). Bistability and Competition of Spatiotemporal Chaotic and Fixed Point Attractors in Rayleigh-Bénard Convection. *Physical Review Letters*, 79(10), 1853–1856. Retrieved 2025-03-25, from <https://link.aps.org/doi/10.1103/PhysRevLett.79.1853> doi: 10.1103/PhysRevLett.79.1853
- Cantwell, C., Moxey, D., Comerford, A., Bolis, A., Rocco, G., Mengaldo, G., . . . Sherwin, S. (2015, July). Nektar++: An open-source spectral/hp element framework. *Computer Physics Communications*, 192, 205–219. Retrieved 2025-03-25, from <https://linkinghub.elsevier.com/retrieve/pii/S0010465515000533> doi: 10.1016/j.cpc.2015.02.008
- Croquette, V. (1989, March). Convective pattern dynamics at low Prandtl number: Part I. *Contemporary Physics*, 30(2), 113–133. Retrieved 2025-03-25, from <http://www.tandfonline.com/doi/abs/10.1080/00107518908225511> doi: 10.1080/00107518908225511
- Decker, W., Pesch, W., & Weber, A. (1994, August). Spiral defect chaos in Rayleigh-Bénard convection. *Physical Review Letters*, 73(5), 648–651. Retrieved 2025-03-25, from <https://link.aps.org/doi/10.1103/PhysRevLett.73.648> doi: 10.1103/PhysRevLett.73.648
- Driscoll, T. A., Hale, N., & Trefethen, L. N. (2014). Chebfun guide.

- (Publisher: Pafnuty Publications, Oxford)
- Geuzaine, C., & Remacle, J. (2009, September). Gmsh: A 3-D finite element mesh generator with built-in pre- and post-processing facilities. *International Journal for Numerical Methods in Engineering*, 79(11), 1309–1331. Retrieved 2025-05-27, from <https://onlinelibrary.wiley.com/doi/10.1002/nme.2579> doi: 10.1002/nme.2579
- Gibson, J. F., Halcrow, J., & Cvitanović, P. (2008, September). Visualizing the geometry of state space in plane Couette flow. *Journal of Fluid Mechanics*, 611, 107–130. Retrieved 2025-04-07, from https://www.cambridge.org/core/product/identifier/S002211200800267X/type/journal_article doi: 10.1017/S002211200800267X
- Jiménez, J., & Moin, P. (1991, April). The minimal flow unit in near-wall turbulence. *Journal of Fluid Mechanics*, 225, 213–240. Retrieved 2025-03-25, from https://www.cambridge.org/core/product/identifier/S0022112091002033/type/journal_article doi: 10.1017/S0022112091002033
- John Soundar Jerome, J., Chomaz, J.-M., & Huerre, P. (2012, April). Transient growth in Rayleigh-Bénard-Poiseuille/Couette convection. *Physics of Fluids*, 24(4), 044103. Retrieved 2025-03-25, from <https://pubs.aip.org/pof/article/24/4/044103/257562/Transient-growth-in-Rayleigh-Benard-Poiseuille> doi: 10.1063/1.4704642
- Kawahara, G., & Kida, S. (2001, December). Periodic motion embedded in plane Couette turbulence: regeneration cycle and burst. *Journal of Fluid Mechanics*, 449, 291–300. Retrieved 2025-04-07, from https://www.cambridge.org/core/product/identifier/S0022112001006243/type/journal_article doi: 10.1017/S0022112001006243
- Khapko, T., Kreilos, T., Schlatter, P., Duguet, Y., Eckhardt, B., & Henningson, D. S. (2016, August). Edge states as mediators of bypass transition in boundary-layer flows. *Journal of Fluid Mechanics*, 801, R2. Retrieved 2025-03-25, from https://www.cambridge.org/core/product/identifier/S0022112016004341/type/journal_article doi: 10.1017/jfm.2016.434
- Ma, D.-J., Sun, D.-J., & Yin, X.-Y. (2006, September). Multiplicity of steady states in cylindrical Rayleigh-Bénard convection. *Physical Review E*, 74(3), 037302. Retrieved 2025-03-25, from <https://link.aps.org/doi/10.1103/PhysRevE.74.037302> doi: 10.1103/PhysRevE.74.037302
- Morris, S. W., Bodenschatz, E., Cannell, D. S., & Ahlers, G. (1993, September). Spiral defect chaos in large aspect ratio Rayleigh-Bénard convection. *Physical Review Letters*, 71(13), 2026–2029. Retrieved 2025-03-25, from <https://link.aps.org/doi/10.1103/PhysRevLett.71.2026> doi: 10.1103/PhysRevLett.71.2026
- Moxey, D., Cantwell, C. D., Bao, Y., Cassinelli, A., Castiglioni, G., Chun, S., ... Sherwin, S. J. (2020, April). Nektar++: Enhancing the capability and application of high-fidelity spectral/h p element methods. *Computer Physics Communications*, 249, 107110. Retrieved 2025-03-25, from <https://linkinghub.elsevier.com/retrieve/pii/S0010465519304175> doi: 10.1016/j.cpc.2019.107110
- Parker, J., & Schneider, T. (2022, June). Variational methods for finding periodic orbits in the incompressible Navier–Stokes equations. *Journal of Fluid Mechanics*, 941, A17.

- Retrieved 2025-05-29, from https://www.cambridge.org/core/product/identifier/S0022112022002993/type/journal_article doi: 10.1017/jfm.2022.299
- Plapp, B. B., & Bodenschatz, E. (1996, January). Core dynamics of multi-armed spirals in Rayleigh-Bénard convection. *Physica Scripta*, *T67*, 111–116. Retrieved 2025-03-25, from <https://iopscience.iop.org/article/10.1088/0031-8949/1996/T67/022> doi: 10.1088/0031-8949/1996/T67/022
- Plapp, B. B., Egolf, D. A., Bodenschatz, E., & Pesch, W. (1998, December). Dynamics and Selection of Giant Spirals in Rayleigh-Bénard Convection. *Physical Review Letters*, *81*(24), 5334–5337. Retrieved 2025-03-25, from <https://link.aps.org/doi/10.1103/PhysRevLett.81.5334> doi: 10.1103/PhysRevLett.81.5334
- Schmid, P. J., De Pando, M. F., & Peake, N. (2017, November). Stability analysis for n-periodic arrays of fluid systems. *Physical Review Fluids*, *2*(11), 113902. Retrieved 2025-03-25, from <https://link.aps.org/doi/10.1103/PhysRevFluids.2.113902> doi: 10.1103/PhysRevFluids.2.113902
- Schneider, T. M., Eckhardt, B., & Yorke, J. A. (2007, July). Turbulence transition and the edge of chaos in pipe flow. *Physical Review Letters*, *99*(3), 034502. Retrieved 2025-03-25, from <http://arxiv.org/abs/nlin/0703067> (arXiv:nlin/0703067) doi: 10.1103/PhysRevLett.99.034502
- Skufca, J. D., Yorke, J. A., & Eckhardt, B. (2006, May). Edge of Chaos in a Parallel Shear Flow. *Physical Review Letters*, *96*(17), 174101. Retrieved 2025-03-25, from <https://link.aps.org/doi/10.1103/PhysRevLett.96.174101> doi: 10.1103/PhysRevLett.96.174101
- Steinberg, V., & Ahlers, G. (n.d.). Pattern Formation and Wave- Number Selection by Rayleigh-Benard Convection in a Cylindrical Container. *Physica Scripta T*.
- Strogatz, S. H. (2018). *Nonlinear Dynamics and Chaos* (??th ed.). CRC Press. Retrieved 2025-05-29, from <https://www.taylorfrancis.com/books/9780429961113> doi: 10.1201/9780429492563
- Tuckerman, L. S., Kreilos, T., Schröbsdorff, H., Schneider, T. M., & Gibson, J. F. (2014, November). Turbulent-laminar patterns in plane Poiseuille flow. *Physics of Fluids*, *26*(11), 114103. Retrieved 2025-03-25, from <https://pubs.aip.org/pof/article/26/11/114103/315350/Turbulent-laminar-patterns-in-plane-Poiseuille> doi: 10.1063/1.4900874
- Viswanath, D. (2007, June). Recurrent motions within plane Couette turbulence. *Journal of Fluid Mechanics*, *580*, 339–358. Retrieved 2025-04-08, from https://www.cambridge.org/core/product/identifier/S0022112007005459/type/journal_article doi: 10.1017/S0022112007005459
- Zheng, Z., Tuckerman, L. S., & Schneider, T. M. (2024a, December). Natural convection in a vertical channel. Part 1. Wavenumber interaction and Eckhaus instability in a narrow domain. *Journal of Fluid Mechanics*, *1000*, A28. Retrieved 2025-11-04, from https://www.cambridge.org/core/product/identifier/S0022112024008425/type/journal_article doi: 10.1017/jfm.2024.842

- Zheng, Z., Tuckerman, L. S., & Schneider, T. M. (2024b, December). Natural convection in a vertical channel. Part 2. Oblique solutions and global bifurcations in a spanwise-extended domain. *Journal of Fluid Mechanics*, 1000, A29. Retrieved 2025-11-04, from https://www.cambridge.org/core/product/identifier/S0022112024008401/type/journal_article doi: 10.1017/jfm.2024.840